Title
Axial Load Transfer Analyses of Energy Piles at a Rock Site

Journal
Geotechnical and Geological Engineering, 38(5)

ISSN
0960-3182

Authors
Moradshahi, Aria
Khosravi, Ali
McCartney, John S
et al.

Publication Date
2020-10-01

DOI
10.1007/s10706-020-01322-5

Peer reviewed

Axial Load Transfer Analyses of Energy Piles at a Rock Site

Aria Moradshahi

Ph.D. Student, Monash University, Department of Civil Engineering,

Clayton, Vic. 3800, Australia; aria.moradshahi@monash.edu

Ali Khosravi, PhD.

Research Associate, Oregon State University, Department of Civil and Construction Engineering, Corvallis, OR

Adjunct Professor, Sharif University of Technology, Department of Civil Engineering

Tehran, Iran; ali.khosravi@oregonstate.edu

John S. McCartney, Ph.D., P.E.

Professor and Department Chair, University of California San Diego, Department of Structural Engineering, La Jolla, CA, USA; mccartney@ucsd.edu

Abdelmalek Bouazza, PhD.

Professor, Monash University, Department of Civil Engineering, Clayton, Victoria, Australia; Malek.Bouazza@monash.edu

Abstract

An axial load-transfer analysis is presented in this study that incorporates empirical models for estimating the side shear resistance and end bearing capacity in rock along with associated normalized stress-displacement curves. The analysis was calibrated using results field experiments involving monotonic heating of three 15.2 m-long energy piles in sandstone. Analyses of the field experiments indicates that poor cleanout of the excavations led to an end restraint smaller than that expected for a clean excavation in sandstone. Specifically, end bearing parameters representative of cohesionless sand were necessary to match the load-transfer analysis to the field experiment results. Parametric evaluations of the analysis demonstrate the importance of using appropriate rock- or soil-specific empirical models when estimating the side shear resistance and end bearing capacity of energy piles. The end bearing capacity and side shear resistance in rock are greater than in soils, leading to more restraint and greater thermal axial stresses. The stiffer side shear restraint in rock was also found to lead to a less nonlinear distribution in thermal axial stress.

Keywords: Energy piles; load transfer analysis; thermo-mechanical loading; rock behavior

List of symbols:

E: Young's modulus of the energy pile

α: Linear thermal expansion coefficient of the energy pile

$\varepsilon_{a,M}$: Mechanical axial strain of the energy pile

$\varepsilon_{a,T}$: Thermal axial strain of the energy pile

σ_a: Axial stress

K_i: Stiffness of the energy pile

l: Length of each element of the energy pile

$Q_{b,max}$: End bearing capacity of the energy pile

$Q_{s,max}$: Side shear resistance of the energy pile

Q_{base}: Reaction force at the base of the energy pile

$\rho^j_{b,M}$: Displacement at the bottom of each element due to mechanical loading

$\rho^j_{t,M}$: Displacement at the top of each element due to mechanical loading

$\rho^j_{s,M}$: Displacement at the side of each element due to mechanical loading

$Q^i_{t,M}$: Mechanical axial force at the top of the energy pile for each element

$Q^i_{b,M}$: Mechanical axial force at the bottom of the energy pile for each element

$Q^i_{s,M}$: Mechanical force at the side of the energy pile for each element

Q^i_{ave}: Average mechanical axial force for each element of the energy pile

Δ^i_M: Mechanical elastic compression of each element of the energy pile

Δ^i_T: Thermal initial expansion/contraction for each element of the energy pile

$\rho^j_{b,T}$: Displacement at the bottom of each element due to thermal loading

$\rho^j_{t,T}$: Displacement at the top of each element due to thermal loading

$\rho^j_{s,T}$: Displacement at the side of each element due to thermal loading

$Q^i_{t,T}$: Thermal axial force at the top of the energy pile for each element

$Q^i_{b,T}$: Thermal axial force at the bottom of the energy pile for each element

$Q^i_{s,T}$: Thermal force at the side of the energy pile for each element

σ^i_T: Average thermal-induced axial stress acting on each element

$Q_{base,T}$: Response of the base of the energy pile due to thermal loading

$Q_{h,T}$: Response of the overlying structure due to thermal loading

$\Delta^i_{T,actual}$: Thermal initial displacement for each element of the energy pile

Ψ: Adhesion factor

q_u: Unconfined compressive strength of rock

1. Introduction

In recent years, reinforced concrete geostructures like piles, walls and slabs have been used as geothermal heat exchangers to access the relatively constant temperature of the ground for efficient heating and cooling of buildings. The thermo-mechanical responses of full-scale energy piles have been evaluated in a range of soil and rock deposits in Europe (Laloui et al. 2003; Brandl 2006; Laloui et al. 2006; Adam and Markiewicz 2009; Bourne-Webb et al. 2009; Wood et al. 2009; Amatya et al. 2012), Japan (Ooka et al. 2007; Hamada et al. 2007), China (Gao et al. 2008, (You et al. 2016), Australia (Bouazza et al. 2011; Wang et al. 2015, Singh et al. 2015, Faizal et al. 2016, 2018a, 2018b, 2019), and the USA (McCartney and Murphy 2012, 2017; Sutman et al. 2014; Akrouch et al. 2014; Murphy and McCartney 2015; Murphy et al. 2015). The soil-structure interaction response and heat exchange capabilities characterized in these studies have generally indicated that energy piles can serve as sustainable geothermal heat exchangers. The main advantage of energy piles is that they help improve the energy efficiency of building space conditioning systems without the need for additional infrastructure or materials beyond that needed to support the building.

Several researchers have evaluated the mechanisms of side shear and end bearing restraint on the thermo-mechanical response of energy piles in soils (Bourne-Webb et al. 2009; Amatya et al. 2012; Goode and McCartney 2015). Different numerical techniques have been developed to interpret the soil-structure interaction in energy piles like the axial load transfer (*T*-*z*) analysis (Knellwolf et al. 2011; Suryatriyastuti et al. 2014; Chen and McCartney 2016; Sutman et al. 2018) and finite element or finite difference methods (Laloui et al. 2006; Ouyang et al. 2011; Gao et al. 2008; Bodas-Freitas et al. 2013; Suryatriyastuti et al. 2013; Olgun et al. 2014a; Wang et al. 2015; Suryatriyastuti et al. 2015; Batini et al. 2015; Khosravi et al. 2016; Bourne-Webb et al. 2016). A comparison of the load-transfer method and finite element modeling was investigated by Abdelaziz and Ozudogru (2016), who found that the load transfer method provides similar results if the proper parameters are selected to capture the soil behavior and restraint of the overlying structure. These numerical techniques have been used in the development of design standards for solitary energy piles (Peron et al. 2011; Burlon et al. 2013; Mimouni and Laloui 2014; Batini et al. 2015), design standards for energy pile groups (Rotta-Loria and Laloui 2017), and to study the effects of cyclic heating and cooling on the behavior of energy piles (Suryatriyastuti et al. 2014; Saggu and Chakraborty 2014; Pasten and Santamarina 2014; Khosravi et al. 2016; Sutman et al. 2018). However, the mechanisms governing the restraint provided by rock on the thermo-mechanical response of energy piles has not been as widely studied, even though there have been some field studies on energy piles in different types of rock (e.g., Murphy and McCartney 2015; Murphy et al. 2015).

An important set of information needed to predict the thermo-mechanical response of energy piles in rock are the distribution in side shear resistance with depth and the end bearing capacity, both of which may be significantly different than those for piles in soil layer. The horizontal stress relief during drilling in rock is not expected to lead to plastic deformations that may result in differences between the interface shear properties inferred from laboratory experiments as is the case of piles in soils. Further, the ultimate capacity of drilled shaft foundations in rock is usually estimated from the unconfined compressive strength of the rock along with adjustments which rely heavily on empiricism (e.g., Seidel and Haberfield 1994). Specifically, several studies have found that the ultimate capacity of piles in rock is related to the ratio of the diameter of the pile to the depth of its embedment, the ratio of the compression modulus of the rock mass to the elastic modulus of the concrete pile, the conditions at the contact between the lateral surface of the pile and rock, and the pile installation procedure (Day 1974; Pells et al. 1978; Horvath et al. 1983; Williams and Pells 1981; Kulhawy and Phoon 1993, Irvine et al. 2014).

This paper describes the formulation and calibration of a numerical method based on the thermo-mechanical axial load transfer method described by Chen and McCartney (2016) to predict the behavior of energy piles in rock during thermo-mechanical loading. Specifically, the analysis in this study considers empirical relationships for variations in the ultimate capacity of piles rock, the shape of the stress-displacement curves, and the role of elastic unloading. The model parameters were calibrated based on the results of in-situ experiments and measurements of axial strains during monotonic heating of three full-scale energy piles located beneath a building at the Air Force Academy in Colorado Springs, CO, USA. The model was then validated using data obtained during monotonic cooling back to the ambient ground temperature. A parametric evaluation of relevant variables in the model was then performed to understand the role of each parameter on the thermo-mechanical response of energy piles in rock. In addition, specific issues investigated include the effects of head stiffness imposed on the pile by the overlying structure, differences expected between energy piles in sand and rock, and the effects of poor cleanout of cuttings from excavations in rock encountered in the construction of the three energy piles evaluated in this study.

2. Model Description

2.1. Terms and Definitions

The axial deformation of an energy pile is complex due to the interaction between the surrounding material (soil or rock) and the pile (reinforced concrete) caused by the differential thermal volume change of the two materials, with a thermo-elastic response expected for the energy pile and a thermo-elasto-plastic response potentially expected for the soil or rock near the pile interface. Initial mechanical loading of the energy pile associated with construction of the overlying building will lead to a given initial deformation distribution within the energy pile due to elastic compression of the pile, and the mobilization of side shear stresses between the soil or rock and the pile. Except in the case of heavily-loaded energy piles (i.e., axial load close to the total axial capacity), the mobilization of side shear stresses is expected to be in the elastic range. Alternatively, if the energy pile is loaded mechanically to a high fraction of its ultimate capacity, ratcheting effects may be encountered leading to plastic deformations during heating and cooling (Pasten and Santamarina 2014).

For an unrestrained energy pile, the thermo-elastic axial strain $\varepsilon_{a,T}$ is assumed to be linearly proportional to changes in temperature ΔT, and can be obtained using the following equation:

$$\varepsilon_{a,T} = \alpha_T \Delta T \quad (1)$$

where α_T is the coefficient of free linear thermal expansion which varies from -8 to -16 με/°C for reinforced concrete (e.g., Bourne-Webb et al. 2009; Murphy and McCartney 2012; Stewart and McCartney 2013; Murphy et al. 2015; Goode and McCartney 2015). The negative sign for α_T implies that a positive change in temperature will lead to thermal expansion (negative strain). Due to restrictions imposed by the side shear resistance and compression strength of the material at the toe, the magnitude of thermal axial strain of an energy pile is expected to be lower than that predicted using Equation (1).

In this study, the load transfer analysis developed by Coyle and Reese (1966) for piles under mechanical load was adapted to investigate the stress and deformation behavior of energy piles in rock during thermo-mechanical loading. Assumptions used in the adaptation of the model include:

1. The Young's modulus (E) of the reinforced concrete pile and its coefficient of free linear thermal expansion (α_T) are constant along the length of the pile.

2. To be consistent with geotechnical sign conventions, compressive stresses and strains are defined as positive, and a downward settlement is defined as positive.
3. The analysis is initiated by discretizing the pile into a series of elements, each represented by a spring of stiffness K_i to describe the deformation behavior of the pile element (Figure 1). K_i for each element was defined based on geometrical aspects of the element, as well as its elastic stiffness characterized using the following equation:

$$K_i = \frac{A_i E_i}{L_i} \quad (2)$$

   where A_i is the cross-section area of element i.
4. The load transfer analysis involves the use of a series of nonlinear stiffness functions referred to as *Q-z* and *T-z* curves to describe the soil-pile interaction. The *Q-z* curve describes the mobilization of end bearing capacity with the displacement of the toe of the pile and the *T-z* curve represents the mobilization of side shear resistance with displacement at a given depth.
5. In load transfer analysis for energy piles, a spring with a stiffness of K_h is added to the head of the pile to represent the restraint imposed by the overlying structure (Knellwolf et al. 2011).

The thermo-mechanical analysis of energy piles in rock was performed following two different steps: the first step involves mechanical loading in which the distribution of axial and interface displacements and forces along the pile for a given initial mechanical load were obtained. The second step involves thermal loading in which the pile response is evaluated during monotonic heating followed by ambient cooling. The indices *M* and *T* stand for mechanical and thermal loading steps.

2.2. Mechanical Loading Step

Although well-established in previous studies (e.g., Coyle and Reese 1966), it is important to clarify that mechanical loading leads to the initial conditions in an energy pile undergoing temperature changes (Chen and McCartney 2016). A schematic of a discretized pile and a typical element for mechanical stress and strain calculations is shown in Figure 1(a). The mechanical loading step starts from element n located at the base of the pile. The analysis is initiated by imposing a value of displacement ρ_{base} on the base of the pile, and determining its reaction force at the base, Q_{base} from the mobilized end bearing curve. Like previous studies on the behavior of conventional piles and energy piles in soil and rock (Randolph and Wroth 1978; Kim et al. 1999; Basarkar and Dewaikar 2006; McCartney and Rosenberg 2011), variations in Q_{base} with base displacement ρ_{base} are described using a hyperbolic equation, as follows:

$$Q_{base} = Q_{b,max} \frac{\rho_{base}}{a_b + b_b \rho_{base}} \quad (3)$$

where $Q_{b,max}$ is the end bearing capacity of the material at the toe of the energy pile, and a_b and b_b are parameters that govern the initial stiffness and nonlinearity of the mobilized force-displacement curve, respectively. Based on Wong and Teh (1995) and Chen and McCartney (2016) b_b can be either 1.0 or 0.9 depending on which would provide a better fit to experimental data, and a_b can be estimated from the hyperbolic curve using the following equation (Wong and Teh 1995):

$$\frac{a_b}{Q_{b,max}} = \frac{1}{k_b} \quad (4)$$

where k_b can be defined as follows (Randolph and Wroth 1978):

$$k_b = \frac{4G_i r_0}{(1 - v_i)} \quad (5)$$

where r_0 is the pile radius, v_i is the Poisson's ratio for a given layer, and G_i is the shear modulus for a given layer which is a function of the Young's modulus and the Poisson's ratio. The *Q*-*z* curve for the element at the toe of the energy pile is defined as the ratio of the mobilized end bearing to the end bearing capacity, which can be obtained from Equation (3) by moving $Q_{b,max}$ to the left-hand side of the equation. A typical shape of the *Q*-*z* curve with the loading path represented by Equation (3) is shown in Figure 2(a). From the calculated base resistance, Q_{base}, the average axial force in each element, Q^i_{ave} is obtained by averaging the axial forces at the top ($Q^i_{t,M}$) and bottom of the element ($Q^i_{b,M}$), as follows :

$$Q^i{}_{ave} = \left(\frac{Q^i{}_{b,M} + Q^i{}_{t,M}}{2}\right) \tag{6}$$

For element n, $Q^n_{b,M} = Q_{base}$ and $Q^n_{t,M}$ is initially assumed to be zero, leading to a value of Q^n_{ave} equal to:

$$Q^n{}_{ave} = \frac{Q_{base}}{2} \tag{7}$$

From the value of Q^n_{ave}, the elastic compression of the bottom element, Δ^n_M, is obtained by dividing the average force, Q^n_{ave}, by the stiffness of the element, K_n, as follows:

$$\Delta^n{}_M = Q^n{}_{ave}/K_n \tag{8}$$

Using the value of Δ^n_M and $\rho^n_{b,M}$, the displacement at the side of the bottom element due to mechanical loading, $\rho^n_{s,M}$, is calculated as follows:

$$\rho^n{}_{s,M} = \rho^n{}_{b,M} + \frac{\Delta^n{}_M}{2} \tag{9}$$

The side shear force mobilized on the side of an element, Q^n_s, is calculated using a hyperbolic *T-z* curve for a given value of $\rho^i_{s,M}$ with the loading path represented as follows:

$$Q^n{}_{s,M} = Q_{s,max}\frac{\rho^n{}_{s,M}}{a_s + b_s\rho^n{}_{s,M}} \tag{10}$$

where $Q_{s,max}$ is the side shear resistance for a given depth along the pile, and a_s and b_s are parameters related to the initial stiffness and the nonlinearity of the mobilized force-displacement curve, respectively. Similar to the end bearing parameters, b_s was assumed to be 0.9, and a_s can be estimated using following equation:

$$\frac{a_s}{Q_{s,max}} = \frac{1}{k_s} \tag{11}$$

where k_s can be defined as follows for each element (Randolph and Wroth 1978):

$$k_{si} = \frac{2\pi G_i l_i}{\ln\left(\frac{r_m}{r_0}\right)} \tag{12}$$

where l_i is pile element length, r_0 is pile radius, and r_m is radius of influence of the pile. Empirical correlations suggested by Lim et al. (1993) show that for pile aspect ratios (L/D) of 25 to 200, r_m generally ranges between 0.5L to 2.5L respectively.

The T-z curve for a given element along the pile interface is defined as the ratio of the mobilized side shear force to the side shear resistance and can be obtained from Equation (10) by moving $Q_{s,max}$ to the left-hand side of the equation. A typical shape for the T-z curve is shown in Figure 2(b). It should be noted that as the load-transfer analysis does not consider the thermal expansion of the surrounding subsurface, the parameters a_s and b_s fitted to a given set of data indirectly account for the relative expansion between the two materials after reaching a given temperature. Results from the finite element analyses of Bodas-Freitas et al. (2013) and Bourne-Webb et al. (2016) indicate that the differential thermal expansions of the pile and soil due to the nonuniform distribution in temperature during heat transfer can lead to changes in the interface stresses between the two materials. A numerical study on energy piles (Olgun et al. 2014a) together with two full-scale field studies energy piles (Faizal et al. 2018a, 2018b) reported no significant changes in pile soil contact stresses due to the radial thermal expansion of the energy pile. The assumption that radial displacements have negligible effects on axial soil-structure interaction has also been confirmed in other studies on load-transfer analysis (e.g., Knellwolf et al. 2011; Chen and McCartney 2016). Therefore, in this study, it was assumed that no interface stresses are generated due to the radial thermal expansion of the energy pile.

From the forces at the bottom and sides of an element, a new value for the force at the top of the element is obtained, as follows:

$$Q^{n}{}_{t,M,new} = Q^{n}{}_{b,M} + Q^{n}{}_{s,M} \tag{13}$$

With the values of Q at the top and bottom of each element, a similar procedure is repeated for other elements to obtain the side shear forces of each element, knowing that for each element, $Q^{i}{}_{b,M}$ of the upper element is equal to $Q^{i}{}_{t,M}$ of the lower element. Equations (6) to (13) are then iterated in the same order until the absolute value of the change in $Q^{n}{}_{t,M,new}$ between different iterations becomes less than a certain value (i.e., a user-defined tolerance), which indicates that equilibrium is satisfied. In this paper, a tolerance of 10^{-10} was used. Convergence occurred typically within 3 to 4 iterations.

2.3. Thermal Loading Step

An energy pile will tend to expand or contract axially during heating and cooling, respectively. However, the tendency for expansion or contraction may be restrained by the surrounding subsurface (side shear resistance or end bearing) and the overlying structure. The degree of restraint will lead to the development of axial forces within the pile, which can be calculated using the adapted load transfer analysis. A schematic of the discretized energy pile and two typical elements located above and below the null point during heating is shown in Figure 1(b). The analysis begins from the null point (denoted as NP), which is the point of zero axial displacement of the energy pile. The location of the null point depends on the stiffness of the overlying superstructure, the stiffness of the material beneath the toe of the pile, and the distribution of mobilized side shear resistance along the pile (Bourne-Webb et al. 2009; Amatya et al. 2012; Olgun and McCartney 2014; Murphy et al. 2015). In this study, equilibrium between forces on each element and compatibility between displacements, ρ, were checked during an iterative process to find the location of the null point in the pile. To start the analysis, an initial guess for the null point was selected as the node at the top of the pile. During heating, the initial displacements and axial force in each element are equal to the values from the mechanical analysis in the previous section. The iterative process was then initiated assuming that the pile is totally free to move at the top and bottom boundaries by an amount corresponding to the free thermal expansion (or contraction), calculated for each element as follows:

$$\Delta_T^i = \alpha_T l_i \Delta T \tag{14}$$

for each element where ΔT is the temperature change, l_i is the length of each element, i is the element number and α_T is the linear coefficient of thermal expansion.

Using the assigned displacements, the thermal analysis was started from the first element below the null point (noted as np+1). This element has a zero displacement at its top (following the null point criterion), but can expand or contract from the bottom during thermal loading with values of displacements that can be obtained from the following equations:

$$\rho_{s,T}^{np+1} = \pm \frac{\Delta_T^{np+1}}{2} \tag{15}$$

$$\rho_{b,T}^{np+1} = \pm \Delta_T^{np+1} \tag{16}$$

where $\rho_{b,T}$ and $\rho_{s,T}$ represent the thermally induced displacements at the base and sides of the element under a temperature change, ΔT. In these equations, the positive values of displacement were used when the pile is heated, and the negative values were used during the cooling period. For other elements below the null point (i=np+2 to n), the displacements for each element can be calculated using the following equations:

$$\rho_{t,T}^i = \rho_{t,T}^{i-1} \tag{17}$$

$$\rho^i_{s,T} = \rho^i_{t,T} \pm \frac{\Delta^i_T}{2} \tag{18}$$

$$\rho^i_{b,T} = \rho^i_{t,T} \pm \Delta^i_T \tag{19}$$

A similar procedure is followed to obtain the displacements of the elements above the null point. It should be noted that the values of displacement obtained using Equations (18) and (19) were for the case of free boundary conditions (the pile is unrestrained and free to move). However, the movement of the pile will be restrained by surrounding subsurface and the overlying structure. To find the actual displacements of the elements, the average thermal-induced axial stress acting in each element is obtained as follows:

$$\sigma^i{}_T = \frac{Q^i{}_{ave}}{A} = \frac{\left(Q^i{}_{t,T} + Q^i{}_{b,T}\right)}{2A} \tag{20}$$

where $Q_{t,T}$ and $Q_{b,T}$ are the axial forces at the top and bottom of the pile, respectively, and are obtained as follows:

$$Q^i_{t,T} = \sum_{j=n}^{i} Q^j_{s,T} + Q_{base,T} \tag{21}$$

$$Q^i_{b,T} = Q^{i+1}_{t,T} \tag{22}$$

In this equation, $Q_{base,T}$ represents the reaction at the base due to the downward expansion of the energy pile and can be obtained from the Q-z curve in Equation (3), and $Q^j{}_{s,T}$ is the shear force on the sides of the pile elements. The determination of $Q^j{}_{s,T}$ is more complex than $Q_{base,T}$. As the initial forces in the thermal analysis are the forces from the mechanical analysis, the upper part of the energy pile above the null point will undergo elastic unloading during heating, while the lower part of the energy pile below the null point will move further downward, leading to further elasto-plastic loading. For the lower part of the energy pile, $Q^j{}_{s,T}$ can be obtained from the T-z curve in Equation (10). For the upper part of the energy pile experiencing elastic unloading, the following equation is used to define the mobilized shear resistance $Q^{j}_{s,T}$:

$$Q^{n}{}_{s} = Q_{s,max}\left[\frac{\rho_s}{a_s} + \frac{Q_{s,i}}{Q_{s,max}} - \left(\frac{1}{\frac{Q_{s,max}}{Q_{s,i}} - b_s}\right)\right] \tag{23}$$

where $Q_{s,i}$ represents the mobilized side shear resistance at a given depth after mechanical loading is applied to the pile head. A typical linear unloading path calculated from Equation (23) is shown in Figure 2(b). For the loading path (Figures 2(a) and 2(b)), it is assumed that the soil-pile contact results in mobilization of side and end-bearing stresses from the beginning of loading, and therefore, a hyperbolic approximation such as Reese and O'Neil (1987) curves can better describe the pile response (Chen and McCartney 2016).

From the values of $\sigma^{i}{}_{T}$ and $\Delta^{i}{}_{T}$, the actual element expansion/contraction for each element can be obtained as follows:

$$\Delta^{i}_{T,actual} = \Delta^{i}_{T} - \frac{\sigma^{i}{}_{T} l_i}{E} \tag{24}$$

where $\sigma^{i}{}_{T}$ is the thermal axial stress in the element and l_i is the length of the element. The actual displacements were then replaced with the initial displacements of free boundary conditions in Equations (14) to (19) to obtain a new set of actual displacements, and this process is repeated until reaching a certain tolerance (reaching a difference of 10^{-10} between the actual displacements of two subsequent iterations). When the final thermally-induced displacements are obtained, they are used to determine the forces at the bottom and side of each element using Equations (3), (10), and (23). For a given assumed location of the null point, equilibrium of forces above and below the null point can be checked as follows (Knellwolf et al. 2011):

$$\left(\sum_{i=1}^{np} Q_{s,T}^{i} + Q_{h,T}\right) = \left(\sum_{i=np+1}^{n} Q_{s,T}^{i} + Q_{base,T}\right) \tag{25}$$

where $Q_{h,T}$ describes the response of the structure at the head of the pile and is assumed to be linearly proportional to the displacement of the pile head. Starting with the node at the top of the pile, the analysis from Equation (14) to (25) is repeated until locating the node at which Equation (24) is satisfied (i.e., the pile is in equilibrium). After locating the null point, which by definition is the point of no thermally induced displacement, the algorithm calculates the thermally-induced displacements and forces in each element in the pile using Equations (14) through (25). When the thermally-induced expansion/contraction of each element is obtained, the thermal axial strains and stresses for each element are calculated as follows:

$$\varepsilon_{T,i} = \frac{\Delta_{T,actual}^{i}}{l_i} \tag{26}$$

$$\sigma_{T,i} = E\left(\varepsilon_{T,i} - \alpha_T \Delta T\right) \tag{27}$$

where $\varepsilon_{T,i}$ is the thermal axial strain at a given depth, E is the Young's modulus of reinforced concrete, α_T is the linear coefficient of free (unrestrained) thermal expansion of reinforced concrete, and ΔT is the temperature change. The temperature change is assumed to be uniform along the length of the energy pile following the observations of studies like Murphy et al. (2015). The mobilized side shear stress as a function of depth can be calculated from the thermal axial stresses as follows:

$$f_{s,mob}^{i} = \frac{\left(\sigma_{T,i} - \sigma_{T,i-1}\right)D}{4\Delta l_i} \tag{28}$$

where Δl_i is the distance between elements *i* and *i*-1.

Analysis of the pile during cooling back to ambient ground temperature can be performed following the same procedure but using the displacements and forces of the elements at the end of the heating process as the starting values for the analysis. During cooling, the bottom element will also experience elastic unloading. The unloading path of the Q-z curve can be expressed as follows:

$$Q^n{}_b = Q_{b,max}\left[\frac{\rho_b}{a_b} + \frac{Q_{b,i}}{Q_{b,max}} - \left(\frac{1}{\frac{Q_{b,max}}{Q_{b,i}} - b_b}\right)\right] \tag{29}$$

where $Q_{b,i}$ represents the mobilized end bearing at the beginning of cooling. For the case where temperature reversals below the ambient conditions are encountered, more complex T-z and Q-z curves should be used, such as those proposed by Knellwolf et al. (2011), Suryatriastuti et al. (2014) or Sutman et al. (2018). A simplified flowchart of the thermal and thermo-mechanical calculation is shown in Figure 3.

3. Parameter Estimation for Energy Piles

There are different approaches to estimate the end bearing capacity and side shear resistance in different geomaterials. The energy piles tested by Murphy et al. (2015) that are analyzed in this study pass through cohesionless soil layers but are socketed in sandstone bedrock, so the ultimate side shear distributions and T-z curve parameters in both soil and rock are needed while in ideal conditions (without the case of poor cleanout of the toe) only the end-bearing capacity and Q-z parameters in rock would be needed.

3.1.Side Shear Resistance

In cohesionless soils, the side shear resistance is assumed to be affected by the installation process due to the stress relief associated with excavation and will vary with depth. The ultimate side shear resistance in cohesionless soils can be estimated using the beta method, given as follows:

$$Q_{s,max} = \sum_{i=1}^{j} \beta\, A_s \sigma_v{}' \tag{30}$$

where σ'_v is the effective vertical stress at the level of the pile base, i represents the element of interest within the pile, β is an empirical reduction factor representing the effects of pile installation, A_s is the surface area of the side of the pile within a given increment of depth.

For drilled shafts in intact rocks, the installation process is assumed to have minor effect on the horizontal displacement response of the rock. Accordingly, the use of Rankine pressure distribution or Coulomb lateral force coefficients may result in overly conservative estimates of the horizontal stresses on piles in sedimentary rock (Ching et al. 2013). Accordingly, the side shear resistances are assumed to be related to the unconfined compressive strength, q_u of the rock (Pells et al. 1978; Horvath et al. 1983; Williams and Pells 1981; and Kulhawy and Phoon 1993), adjusted by an empirical α parameter to account for installation effects (interface smoothness, etc.). For example, Kulhawy and Phoon (1993) developed a general expression for the side shear resistance based on data from load tests on piles in rock reported by Rowe and Armitage (1989), Bloomquist et al. (1991), and McVay et al. (1992), as follows:

$$Q_{s,max} = \Psi \times {q_u}^{0.5} \tag{31}$$

where q_u is the unconfined compressive strength of rock and Ψ is an empirical adhesion factor to account for the lower interface shear strength compared to the compressive strength of the intact rock. Kulhawy and Phoon (1993) found that the value of Ψ ranges from 0.112 for claystone, 0.224 for shale and mudstone, 0.448 for shale (rough socket), to 0.672 for sandstone, limestone and marl. Similar empirical equations for the side shear resistance of piles were proposed by Cole and Stroud (1976).

3.2.End-bearing Capacity

The end-bearing capacity of energy piles embedded in a rock depends on the quality of cleanout of cuttings at the toe of the excavation. In an ideal situation with complete cleanout, the end bearing capacity of a pile in rock can be approximated using the recommendation by Goodman (1989) in terms of the unconfined compressive strength of rock, as follows:

$$Q_{b,max} = q_u(N_\phi + 1)A_b \tag{32}$$

where A_b is the area of the base of the pile and N_ϕ is defined as follows:

$$N_\phi = tan^2(45 + \phi'/2) \tag{33}$$

In the case that there is poor cleanout of the toe of the excavation in rock, it may not be appropriate to use Equation (32) to estimate the end-bearing capacity (Murphy et al. 2015). Specifically, the toe of the excavation may be filled with cuttings. For the case of sandstone, the cuttings can be assumed to be cohesionless soil. Accordingly, the ultimate end-bearing capacity can be estimated by assuming that the toe of the excavations is filled with cohesionless soil, as follows (Bowles 1968):

$$Q_{b,max} = \sigma'_v N_q A_b \tag{34}$$

where N_q is the bearing capacity factor, A_b is the area of the base of the pile, and σ_v' is the in-situ vertical stress at the depth of the pile base.

In the load transfer analyses of energy piles, some common assumptions are considered:

1- Geomaterials with unconfined compressive strength values ranging from 400 kPa (hard soils) to 2000 kPa (weak rock) can be described as having a transitional behavior (Seidel and Haberfield 1994). For these materials, a more advanced method for estimating $Q_{s,max}$ than those given in Equation (31) for rock or Equation (30) for cohesionless soil is needed.

2- The side shear resistance and end bearing capacity are not sensitive to temperature (Knellwolf et al. 2011; Chen and McCartney 2016), which was verified through thermal borehole shear experiments in cohesionless soil (Murphy and McCartney 2014). Although this assumption is followed in this study for cohesionless soils and rock, it may require further validation for clay and claystone where heating may lead to permanent contraction of the soil and rock if sufficient time is permitted for drainage. This may lead to effects such as thermal dragdown (e.g., McCartney and Murphy 2017).

3- It is a common assumption in current load transfer analysis methods that the piles mostly deform axially and possible effects of radial expansion during heating on their behavior and shear resistance was ignored. This assumption is based on the numerical and field studies considering cavity expansion analysis (Olgun et al. 2014; Zhou et al. 2016; Faizal et al. 2018a, 2018b) in which the effect of pile radial expansion in soil was observed to be negligible. Also, the experimental observations by Mimouni and Laloui (2014) showed blocked radial thermal strains within the stiff soil and rock layers, increasing the axial mobilized thermal expansion by 50%.

4. Model Calibration/Validation

The calibration/validation process of the proposed numerical approach includes the use of the results from the monotonic heating and cooling of three piles installed beneath a one-story building at the Field Engineering and Readiness Laboratory (FERL) of the US Air Force Academy, Colorado Springs, CO, described by Murphy et al. (2015). The thermal loading considered in this study consisted of a cycle of heating and cooling with a change in temperature of ±19 °C from the mean ground temperature of 10 °C under a constant vertical mechanical load of 400 kN (associated with the dead weight of the building). During this cycle, the pile temperature was incrementally elevated to an average temperature of 28 °C in increments of 6 °C then decreased in two steps back to the ambient ground temperature. The results of the tests during the heating cycle were used for the calibration process and estimation of the model parameters. Then, the parameters of the model obtained from the calibration process were used to predict the response of piles during ambient cooling to provide a preliminary validation check on the parameters.

4.1. Energy Piles and Site Description

The energy piles are part of a supporting system of a one-story building, and each have a depth of 15.2 m and a diameter of 0.61 m, arranged in the plan-view layout shown in Figure 4(a). The depth of the energy piles was not defined based on the load-bearing requirements of the building, but to demonstrate the heat transfer response of the system. Of the eight energy piles shown in Figure 4(a), this study focuses on the response of Energy Piles 1, 3, and 4. Each of these piles had two U-loop HDPE heat exchanger pipes distributed in the same manner around the inner perimeter of the reinforcement cage as shown in Murphy et al. (2015), and included embedded instrumentation for the measurement of pile response during loading and temperature changes.

The subsurface stratigraphy of the site is shown in Figure 4(b). The site consists of a 1 m-thick layer of medium dense, sandy fill with silt and gravel underlain by a 1 m-thick medium dense sandy-silty gravel layer underlain by sandstone bedrock extending to a depth below the toes of the energy piles. The geotechnical properties and unit weights of the subsurface layers are presented in Table 1. The unit weight of the reinforced concrete was assumed to be 25 kN/m3, and the subsurface was assumed to be dry as the water table was not encountered during installation of the energy piles. The advantage of evaluating this site using T-z analysis is that the different strata at the site are relatively stiff, and it is assumed that the material will not experience permanent thermo-mechanical volume changes during temperature cycles. The standard penetration test

(SPT) N-values for the subsurface materials are also presented in Table 1. The results of SPT penetration tests along with recommendations provided Stamatopoulos and Kotzas (1985) were used to estimate the unconfined compressive strength of the sandstone. The parameters such as cohesion, friction angle, elastic modulus, and Poisson's ratio were estimated based on recommendations of Bowles (1968) and Mitchell and Soga (2005) for different soils in this study.

Instrumentation was incorporated into the energy piles to measure the axial strain and temperature during thermo-mechanical loading at the locations shown in Figure 4(b). The axial strain distributions with depth in the energy piles were measured using a set of Geokon Model 4200 vibrating wire strain gauges (VWSGs), with six in Piles 1 and 3 and twelve in Pile 4. At three locations within Pile 4, gauges were located at the same depth on opposite sides of the reinforcing cage to gain redundancy in temperature and strain readings and to capture any differential strain measurements across the width of the shaft. Measurements from these sensors were not presented in this paper. These vibrating wire strain gages also include embedded thermistors for monitoring the concrete temperature. A series of ten Geokon model 3810 thermistor strings were also used for monitoring temperature variations in the soil surrounding the energy pile. The measured temperature profiles in Piles 1, 3 and 4 at different instances in time during heating and cooling are shown in Figure 5, along with the average changes in pile temperature at these times. The temperature distribution with depth is relatively constant, except for depths below 11 m where slightly lower temperatures were observed due to heat loss from the toe of the piles. In order to calculate the thermal axial strains, following equation was used (Murphy et al 2015):

$$\varepsilon_T = (\varepsilon_i - \varepsilon_0)B + \alpha\Delta T \tag{35}$$

where ε_i is the measured axial strain at time i, and ε_0 is the initial value of axial strain at the end of building construction, B is the batch calibration factor (taken as 0.975), ΔT is the temperature change between initial value and the value at time i, and α is the coefficient of thermal expansion of the steel wire which is equal to 12.2 $\mu\varepsilon$/°C.

4.2.Methodology for Model Calibration

In order to calibrate the load transfer analysis for the piles in rock, the values of $Q_{s,max}$ for each of the layers were first estimated using the geomaterial properties given in Table 1 (i.e., using Equation (30) for the cohesionless soils layers and Equation (31) for the sandstone), and were assumed to be the same for all three piles as they pass through the same soil layers. A value of Ψ=0.672 for sandstone was estimated based on the recommendations of Kulhawy and Phoon (1993). Estimation of the value of $Q_{b,max}$ was more complex. Murphy et al. (2015) indicated that the drilling contractor did not use a bucket auger to remove the loose cuttings after drilling the hole to the target depth. Due to the poor cleanout of material from the toe of the excavation, Equation (34) was used to estimate the ultimate end-bearing capacity assuming that the cuttings at the toe of the excavation were sand having similar characteristics to the near-surface layers. All three piles were assumed to have the same value of α_T = -13 με/°C for free thermal expansion under unrestrained conditions, consistent with the value used by Murphy et al. (2015) in the interpretation of their results.

A methodology similar to Chen and McCartney (2016) was used to define the properties of soils surrounding the pile such as a_s, b_s, a_b, b_b, and the stiffness of the overlying structure, K_h. This methodology relies on both characteristics of soil and pile as well as the axial stress and strain measurements for soils under different cycles of heating and cooling. The values of b_s and b_b are the failure ratio parameters which describe the ratio of mobilized shaft/end bearing resistance to ultimate shaft/end bearing capacity and are in the range of 0.9 to 1 (McCartney and Rosenberg 2011). In this study, a value of 0.9 was considered for both b_s and b_b. The values of a_s and a_b estimated using Equations 11, 12 and 4, 5 respectively. Since a case with poor toe cleanout was considered for the piles analyzed in this study, a value of a_b = 0.000002 was estimated which is similar to what suggested by Chen and McCartney (2016). In this regard, the results of the tests on energy piles presented by Murphy et al. (2015) during heating were used. The calibrated parameters are summarized in Table 2. These values are in the range proposed by Chen and McCartney (2016) (Table 3).

The results of the calibration process for Piles 1, 3, and 4 during heating are shown in Figures 6 and 7 for the distributions in thermal axial strain and thermal axial stress with depth, respectively. The numerical method and in-situ measurements show that the thermal axial stress initially increases with depth for each of the piles, although the stress starts to decrease below a depth of 9 m in each of the piles (i.e. the approximate location of the null point). As K_h is the only parameter with no information available for (Knellwolf 2011), it was estimated using the following equation by considering a rigid vertically loaded plate (Gorbunov-Posadov & Serebrjanyi 1961; Randolph 1994):

$$K_h = \frac{E_s\sqrt{B_h L_h}}{(1 - v_s^2)\rho_0} \tag{36}$$

where E_s and v_s is the soil Young's modulus and Poisson's ratio respectively, $B_h$and L_h are the slab dimension, and $\rho_0$is the displacement coefficient which can be evaluated as a function of the ratio $\chi = L_h / B_h$suggested by Gorbunov-Posadov and Serebrjanyi (1961).

Values of K_h ranged between 2.0 GPa/m and 2.8 GPa/m based on pile location and soil properties. The results also confirm that the value of K_h for Pile 3 was different from those of Piles 1 and 4 as Pile 3 is located at the corner of the building and has a lower amount of head restraint. Specifically, a value of K_h = 2 GPa/m was selected for Pile 3 (with the slab dimensions of B_h =2.5 m and L_h =5 m) to fit the field data, which is lower than that of the values of K_h of 2.8 GPa/m for Piles 1 and 4 (with the slab dimensions of B_h =5 m and L_h =5 m) for sand and rock cases respectively.

Due to this lower value of K_h the thermal axial stresses are lower in Pile 3. Consistent with the observation of Murphy et al. (2015) that the toes of the excavations may have been poorly cleaned out and are filled with sand cuttings, relatively high values of thermal axial strain are observed at the base of the energy piles. Based on the hypothetical trends noted in Amatya et al. (2012), it would be expected that the thermal axial strains would be small near the toe of an energy pile embedded in a very stiff material like sandstone.

The results in Figure 6 indicate that the thermal axial strains become more negative with increasing changes in temperature, indicating expansion of the pile. Because of mobilization of shear resistance along the pile, a nonlinear distribution in thermal strain was observed with depth during monotonic heating. The location of the null point was captured well by the numerical model using the calibrated parameters. The thermal axial strain profiles start to decrease in magnitude to a depth of about 9 m (the location of the null point), after which the thermal axial strain decreases with further increase in depth. The thermal axial strain profiles of in-situ data show a slight increase in magnitude in depths lower than 2 m (first layer), which was not observed in the model predictions. This behavior could be either due to the deviations in temperatures at these depths from the rest of the pile due to ambient surface temperature fluctuations.

4.3.Validation Results

Although independent data is not available for validation of the model, the parameters of the model were used to predict the response during ambient cooling to provide a preliminary validation check on the parameters. The predictions of the model with the data collected during cooling of the three energy piles are shown in Figures 8 and 9 for the distributions in thermal axial strain and thermal axial stress with depth, respectively. The energy piles will follow a different unloading path during cooling (see Figure 2), so the good fit observed in these figures indicates the validity of the model in capturing other aspects of energy pile behavior than just monotonic heating. Some discrepancies specifically at the middle depths of the energy pile can be related to the simplifications attributed to the load-transfer method such as assuming the shape of the *Q*-*z* and *T*-*z* curves and ignoring thermal deformation of the surrounding ground.

4.4. Sensitivity Analysis

A parametric evaluation was performed to evaluate the sensitivity of the model to key input parameters governing the stiffness of the system, including a_s, a_b and K_h. As these parameters are expected to be independent, the effect of each parameter is investigated separately.

- *Effect of shaft friction parameter (a_s)*

To investigate the effect of the mobilized side shear resistance on the thermo-mechanical response of the energy piles, four different values were considered for the a_s parameter, changing from 0.000002 m (sandstone or stiff soil) to 0.000005 m (soft soil). As shown in Figure 10(a), smaller values of a_s led to greater stresses near the middle of the energy pile as this term reflects the slope of the T-z curve. This observation is similar to the results presented by Mimouni and Laloui (2016) where due to radial blocked thermal strain, piles in stiff soil had higher mobilized side shear stress measured along the pile's length It is interesting to observe that changes in a_s did not lead to changes in the magnitude of stress near the toe and head of the energy pile, where the stress depends more on the parameters governing the end bearing stiffness (a_b**)** and the head-structure stiffness (K_h), which remained unchanged and equal to 0.00004 m and 2.8 GPa/m, respectively.

- *Effect of end bearing parameter (a_b)*

To investigate the effect of the mobilized end bearing capacity on the thermo-mechanical response of the energy piles, four different values in the range of 0.00001 m to 0.00004 m were considered for the a_b parameter. For this analysis, values of 0.000005 m and 2.8 GPa/m were considered for a_s and K_h, respectively. As shown in Figure 10(b), smaller values of a_b led to greater stress values near the toe of the pile. Ideally, rock would be expected to have a lower a_b value, but this may be lower in the case of poor cleanout of the toe.

- *Effect of pile head-structure stiffness (K_h)*

The impact of overlying structure stiffness on the behavior of the energy pile was explored by changing the value of pile head-structure stiffness K_h by using different slab dimensions (Equation 36) Values of a_s and a_b equal to 0.000005 m and 0.00001 m, respectively, were used in this analysis. As shown in Figure 10(c), increasing K_h from 0 (no head restraint) to 6 GPa/m results in significant increases in the stress throughout the pile. This variable also has a major effect on the location of the null point (i.e., the null point tends to move upward as K_h increases). As K_h is not related to soil parameters, it can only be calculated using a structural analysis or from calibration of a load transfer model to measured strain data like in this study.

5. Evaluation of Aspects of Energy Pile Behavior in Rock

The calibrated parameters from the load transfer analysis are useful to evaluate various aspects of energy pile behavior in rock, and how this behavior may be different from soils. The calibrated parameters reflect the fact that the sandy layers overlying the sandstone bedrock led to a change in behavior, and the softer response than expected at the toes of the foundations may be due to poor cleanout of the excavations (in which case there is soil at the toe of the excavations). This section evaluates the differences in thermal axial strains and stresses for energy piles in cohesionless soil and rock to understand the differences in behavior that can be expected for rock and to better interpret the data measured from the field site. Specifically, three cases of load transfer parameters are considered to simulate the behavior of Pile 4:

- ***Case 1***: *Pile in rock with poor toe-cleanout (real case)*

Simulation of Pile 4 using the calibrated load-transfer parameters summarized in Table 2. This case includes T-z curve and ultimate side shear capacity parameters calibrated to represent the restraint provided by the upper cohesionless soil layers and the underlying sandstone bedrock, and Q-z curve and ultimate end-bearing capacity parameters calibrated to represent the restraint provided by the sand cuttings at the toe of the excavation.

- ***Case 2***: *Pile in cohesion-less soil*

Simulation of Pile 4 using the load-transfer properties representative of cohesionless soil as summarized in Table 3. This case includes T-z curve and ultimate side shear capacity parameters representative of cohesionless soil layers throughout the length of the pile, and Q-z curve and ultimate end-bearing capacity parameters representative of the sand cuttings at the toe of the excavation which in this case are the same as those in Case 1. The ultimate side shear distribution with depth for the cohesionless soil layer was calculated using Equation (30), and the end bearing capacity for cohesionless soil was calculated using Equation (34).

- ***Case 3***: *Pile in rock with intact bedrock*

Simulation of Pile 4 using the load-transfer properties representative of intact sandstone bedrock summarized in Table 4. This case includes T-z curve and ultimate side shear capacity parameters representative of rock throughout the length of the pile, and Q-z curve and ultimate end bearing capacity parameters representative of intact sandstone. The Q-z curve parameter a_b for intact bedrock was estimated to be half of the calibrated value in Table 2, which is consistent with the difference in magnitude of end-bearing and semi-floating centrifuge-scale energy piles in Bonny silt simulated by Chen and McCartney (2016). The ultimate side shear capacity was assumed to be uniform with depth according to Eq. (31) and the ultimate end bearing of the energy pile in intact rock was estimated using Equations (32) and (33) with the unconfined compressive strength for sandstone from Table 1.

5.1. Differences in Behavior between Energy Piles in Soil and Rock

Profiles of thermal axial strain and thermal axial stress for energy piles in sand (Case 2) are shown in Figures 11(a) and 11(b), respectively. Comparing the profiles of thermal axial strain and stress for this case with those calibrated against the experimental data for thermal axial strain and thermal axial stress (Case 1) in Figures 6 and 7, respectively, it is observed that the null point location for energy piles in cohesionless soil is higher (around 7 m) due to the lower side shear resistance in the section of the pile that is in rock. Specifically, compared to rocks, the value of a_s for soils is lower which indicates more nonlinearity in axial stress and strain distribution, while the value of a_b is representative of soils and results in a soft base reaction. Different from Case 1, the assumption that the pile was fully embedded in sand in Case 2 led to much larger thermal axial strains near the toe of the pile despite having the same end restraint boundary conditions.

Profiles of thermal axial strain and thermal axial stress for energy piles in ideal, intact sandstone (Case 3) are shown in Figures 12(a) and 12(b), respectively. These profiles highlight the effect of poor cleanout of material from the toe of the excavation. Different from the results shown in Figures 6, 7, and 8, the thermal axial strains at the toe of the energy pile are smaller, and the change in thermal axial strain with depth is less significant due to the uniform distribution of ultimate side shear resistance with depth. Higher values of thermal stress are mobilized near the toe of the energy pile in this case due to the greater restraint, and overall the thermal axial stresses in the pile in intact rock are nearly double that observed in the experimental results in Figure 7. Comparison of the thermal axial stresses in Figures 7 and 12(b) emphasizes the effects of poor cleanout of cuttings from the toe of the excavation: the ultimate capacity of the foundation decreased significantly due to the lower ultimate end bearing, but the thermal axial stresses were also lower. This analysis indicates that the thermal axial stresses observed by Murphy et al. (2015) are likely much lower than what they could have been if the toes of the excavation were carefully cleaned out. As these thermal axial stresses are already a large fraction of the ultimate compressive strength of the concrete, a stronger concrete mix design may need to be used to meet structural stability requirements.

The experimental and numerical profiles of side shear resistance for Piles 1, 3, and 4 are compared in Figure 13(a). The experimental profiles of side shear stresses were obtained by first calculating the axial stresses at each depth using the axial strain values obtained from strain gauges (Equation (35)), which were then used in Equation (27) to calculate the thermal axial stress, which was then used in Equation (28) to calculate the mobilized side shear resistance between each of the sensor locations. The numerical profiles of side shear resistance were calculated using Equation (28) with the thermal axial stresses obtained from the thermo-mechanical load transfer analysis with the calibrated parameters presented in Table 2. The profiles of side shear resistance for the three energy piles follow a similar nonlinear distribution with depth during heating. The side shear resistance profiles show an initial decrease in magnitude at some depths, after which it decreases with further increase in height. This indicates the head stiffness may have an effect on the mobilization of side shear resistance during heating by preventing sufficient displacement for mobilization. Based on the data presented in Figure 13(a), all profiles show a point of zero side shear resistance at a depth of 9 m which corresponds to the location of the null point. The profiles of mobilized side shear resistance along the shaft of Pile 4 are compared in Figure 13(b) for the three cases. In-situ experimental measurements for Pile 4 are also presented in this figure for comparison. For the pile in soil, the location of zero side shear resistance is closer to the surface and a higher value of side shear resistance is mobilized near the toe. The maximum value of mobilized side shear stress at the pile-rock interface did not exceed 45 kPa, while this value reached a value of around 90 kPa at the pile-soil interface. Comparing the results for the cases with proper cleanout of the toe of the rock excavation (Case 3) and with poor cleanout of the toe of the rock excavation (Case 1), lower side shear resistances are observed at the toe for the case with base cleanout, with the null point located at a deeper depth.

6. Conclusion

This study describes the lessons learned from axial load transfer (T-z) analyses of the thermo-mechanical response of energy piles in rock. The model was then calibrated using in-situ measurements of the load and deformation experienced by full-scale energy piles embedded in rock during temperature changes. The load transfer analysis was conducted to provide a good estimation of thermally-induced axial stresses and strains of the energy pile during of monotonic heating and ambient cooling, especially when accounting for the fact that poor cleanout of the excavations likely occurred during construction. The head stiffness, as well as the parameters governing the stiffness at the toe of the energy piles, were observed to play the most significant roles in the magnitudes of thermal axial stress in the energy piles in rock. A comparison using the calibrated parameters with calibrated parameters representative of energy piles in uniform sand and rock layers indicates that a significant difference in the distribution in the magnitude of the thermal axial strain and thermal axial stress can be expected for energy piles in sand or rock layers. The comparison emphasizes the importance of accurately defining the ultimate side shear distribution and ultimate end-bearing capacities of the energy pile to obtain the shapes and magnitudes of the thermal axial stress profiles for different changes in temperature. Greater magnitude of thermal axial stresses with a uniform distribution in depth can be expected for energy piles in rock. Poor cleanout of cuttings from the toes of the excavations in rock was found to have a significant effect on the magnitude of thermal axial stress in the energy piles evaluated in this study, which may indicate that toe cleanout should be carefully considered in the analysis of energy piles in rock.

7. Acknowledgements

J.S. McCartney acknowledges support from DoD ESTCP project EW-201153 and NSF project CMMI-0928159. The views in this paper are those of the authors alone.

References

Abdelaziz S, Ozudogru TY (2016). "Non-uniform thermal strains and stresses in energy piles." Environmental Geotechnics. 3(4), 237-252.

Adam D, Markiewicz R (2009). "Energy from earth-coupled structures, piles, tunnels and sewers." Géotechnique. 59(3), 229-236

Akrouch G, Sanchez M, Briaud J-L (2014). "Thermo-mechanical behavior of energy piles in high plasticity clays." Acta Geotechnica. 9(3), 399–412.

Amatya BL, Soga K, Bourne-Webb PJ, Amis T, Laloui L (2012). "Thermo-mechanical behaviour of energy piles." Géotechnique. 62(6), 503–519.

Basarkar SS, Dewaikar DM (2006). "Load transfer characteristics of socketed piles in Mumbai region." Soils and Foundations. 46(2), 247-257.

Batini N, Rotta Loria AF, Conti P, Testi D, Grassi W, Laloui L (2015). "Energy and geotechnical behaviour of energy piles for different design solutions." Applied Thermal Eng. 86, 199-213.

Bloomquist D, Townsend FC, Parra F (1991). Development of In Situ Equipment for Capacity Determinations of Deep Foundations in Florida Limestone. Final Report for Florida Department of Transportation. Department of Civil Engineering, University of Florida.

Bodas Freitas TM, Cruz Silva F, Bourne-Webb PJ (2013). "The response of energy foundations under thermo-mechanical loading." Proc. 18th International Conference on Soil Mechanics and Geotechnical Engineering. Paris, France. vol. 4, pp. 3347–3350.

Bouazza A, Singh RM, Wang B, Barry-Macaulay D, Haberfield C, Chapman G, Baycan S, Carden Y (2011). "Harnessing onsite renewable energy through pile foundations." Australian Geomechanics Journal. 46(4), 79-90.

Bourne-Webb PJ, Bodas Freitas TM, Freitas Assunção RM (2016). "Soil–pile thermal interactions in energy foundations." Géotechnique. 66(2), 167–171.

Bowles, JE (1968). Foundation Analysis and Design. 5th Edition. McGraw-Hill, New York.

Brandl H (2006). "Energy piles and other thermo-active ground structures." Géotechnique. 56(2), 81-122.

Burlon S, Habert J, Szymkievicz F, Suryatriyastuti M, Mroueh H (2013). "Towards a design approach of bearing capacity of thermoactive piles." European Geothermal Congress 2013. Pisa, Italy. pp. 1-6. (CD-ROM).

Chen Y-J, Kulhawy FH (1994). Case History Evaluation of the Behavior of Drilled Shafts Under Axial and Lateral Loading, Report TR-104601, Electric Power Research Institute, Palo Alto.

Chen D, McCartney JS (2017). "Parameters for load transfer analysis of energy piles in uniform non-plastic soils." International Journal of Geomechanics, 17(7), 04016159.

Ching J, Yang ZY, Shiau JQ, Chen CJ (2013). "Estimation of rock pressure during an excavation/cut in sedimentary rocks with inclined bedding planes." Struct. Safety, 41, 11-19.

Coyle HM, Reese LC (1966). "Load transfer for axially loaded piles in clay." Proc. American Society of Civil Engineers, New York, NY. 92(SM2), 1-26.

Cole KW, Stroud MA (1976). "Rock socket piles at Coventry Point, Market Way, Coventry."

Géotechnique. 26(1), 47–62

Faizal M, Bouazza A, Singh RM (2016). “An experimental investigation of the influence of intermittent and continuous operating modes on the thermal behaviour of a full scale geothermal energy pile.” Geomechanics for Energy and the Environment. 8, 8-29.

Faizal M, Bouazza A, Haberfield C, McCartney JS (2018a). “Axial and radial thermal responses of a field scale energy pile under monotonic and cyclic temperatures.” Journal of Geotechnical and Geoenvironmental Engineering. 144(10), 04018072.

Faizal M, Bouazza A, McCartney JS, Haberfield C (2018b). “Axial and radial thermal responses of an energy pile under a 6-storey residential building.” Canadian Geotechnical Journal. 56(7), 1019–1033. doi:10.1139/cgj-2018-0246.

Faizal M, Bouazza A, McCartney JS, Haberfield C (2019). “Effects of cyclic temperature changes on the thermal response of an energy pile under a residential building.” Journal of Geotechnical and Geoenvironmental Engineering. 145(10): 04019066.

Gao J, Zhang X, Liu J, Li K, Yang J (2008). “Numerical and experimental assessment of thermal performance of vertical energy piles: an application.” Applied Energy. 85(10), 901–910.

Goode JC, McCartney JS (2015). “Centrifuge modeling of boundary restraint effects in energy piles.” Journal of Geotechnical and Geoenvironmental Engineering. 141(8), 04015034-1-04015034-13. DOI: 10.1061/(ASCE)GT.1943-5606.0001333.

Goodman RE (1989). Introduction to Rock Mechanics. 2nd Edition. Wiley, New York.

Gorbunov-Posadov MI, Serebrjanyi RV (1961). “Design of structures on elastic foundation.” In 5th International Conference on Soil Mechanics and Foundation Engineering. Vol. 1, 643-648.

Hamada Y, Saitoh H, Nakamura M, Kubota H, Ochifuji K (2007). “Field performance of an energy pile system for space heating.” Energy and Buildings. 39(5), 517–524.

Hassanzadegan A, Zimmermann G (2014). “A poroelastic description of permeability evolution.” Pure and Applied Geophysics. 171(7), 1187-1201.

Horvath RG, Kenney TC, Kozicki P (1983). “Methods of improving the performance of drilled piers in weak rock.” Canadian Geotechnical Journal. 20(4), 758-772.

Laloui L, Moreni M, Vulliet L (2003). Comportement d'un pieu bi-fonction, fondation et échangeur de chaleur. Canadian Geotechnical Journal. 40(2), 388-402

Laloui L, Nuth M, Vulliet L (2006). “Experimental and numerical investigations of the behaviour of a heat exchanger pile” International Journal for Numerical and Analytical Methods in Geomechanics. 30, 763-781.

Laloui N, Nuth M (2006). “Numerical modeling of some features of heat exchanger pile. Pile Analysis and Design: Innovative Methods” (GSP 153). ASCE. Reston, VA. 189–195.

Lim CH, Chow YK, Karunaratne GP (1993). “Negative skin friction on single piles in a layered half-space.” International Journal for Numerical and Analytical Methods in Geomechanics. 17, 625-645.

Kim KN, Lee SH, Kim K-S, Chung C-K, Kim MM, Lee HS (2001). “Optimal pile arrangement for minimizing differential settlements in piled raft foundation.” Computers and Geotechnics. 28(2), 235-253.

Khosravi A, Moradshahi A, McCartney JS, Kabiri M (2016). “Numerical analysis of energy piles under different boundary conditions and thermal loading cycles.” Proc. 3rd European Unsaturated Soils Conference. EDP, Paris, Sciences. 1-6.

Knellwolf C, Peron H, Laloui L (2011). “Geotechnical analysis of heat exchanger piles.” Geotechnical and Geological Engineering. 137(12), 890–902

Kulhawy FH, Phoon, KK (1993). “Drilled shaft side resistance in clay soil to rock.” Design and

Performance of Deep Foundations: Piles and Piers in Soil and Rock, ASCE GSP 38, 172-183.

McCartney JS, Rosenberg JE (2011). "Impact of heat exchange on the axial capacity of thermo-active piles." Proc. Geo-Frontiers 2011 (GSP 211). Han J, Alzamora DE (eds.) ASCE, Reston, VA, pp 488-498.

McCartney JS, Murphy KD (2012). "Strain distributions in full scale energy piles." DFI Journal. 6(2), 28–36

McCartney JS, Murphy KD (2017). "Investigation of potential dragdown/uplift effects on energy piles." Geomechanics for Energy and the Environment. 10(June), 21-28.

McVay MC, Townsend FC, Williams RC (1992). "Design of socketed drilled shafts in limestone." Journal of Geotechnical Engineering. 118(10), 1626-1637.

Mitchell JK, Soga K (2005). Fundamentals of Soil Behavior. 3rd Edition. Wiley, New Jersey.

Mimouni T, Laloui L (2014). "Towards a secure basis for the design of geothermal piles." Acta Geotechnica. 9(3), 355–366.

Mosher RL, Dawkins WP (2000). Theoretical Manual for Pile Foundations, Report ERDTC/ITL TR-00-5, US Army Corps of Engineers, Washington, DC.

Murphy KD, McCartney JS (2014). "Thermal borehole shear device." ASTM Geotechnical Testing Journal. 37(6), 1040-1055.

Murphy KD, McCartney JS (2015). "Seasonal response of energy piles during building operation." Geotechnical and Geological Engineering. 33(2): 343-356

Murphy KD, McCartney JS, Henry KS (2015). "Evaluation of thermo-mechanical and thermal behavior of full-scale energy pile." Acta Geotechnica. 10(2), 179-195.

Ng CWW, Shi C, Gunawan A, Laloui L (2014). "Centrifuge modelling of energy piles subjected to heating and cooling cycles in clay." Géotechnique Letters 4, 310–316.

Olgun GC, McCartney JS (2014). "Outcomes from the International Workshop on Thermoactive Geotechnical Systems for Near-Surface Geothermal Energy: From Research to Practice." The Journal of the Deep Foundation Institute. 8(2), 58-72.

Olgun CG, Ozudogru TY, Abdelaziz SL, Senol A (2014a). "Long-term performance of heat exchanger pile groups." Acta Geotechnica. 10(5):553-569.

Olgun CG, Ozudogru TY, Arson CF (2014b). "Thermomechanical radial expansion of heat exchanger piles and possible effects on contact pressures at pile-soil interface." Géotechnique Letters. 1-8. DOI: http://dx.doi.org/10.1680/geolett.14.00018.

Ooka R, Sekine K, Mutsumi Y, Yoshiro S, SuckHo H (2007). "Development of a ground source heat pump system with ground heat exchanger utilizing the cast-in place concrete pile piles of a building." EcoStock 2007. pp 1–11.

Ouyang Y, Soga K, Leung YF (2011). "Numerical back-analysis of energy pile test at Lambeth College, London." Geo-Frontiers 2011, Dallas, TX, pp 440–449.

Pasten C, Santamarina JC (2014). Thermally induced long-term displacement of thermoactive piles. Journal of Geotechnical and Geoenvironmental Engineering. 140(5), 06014003.

Pells PJN, Douglas DJ, Rodway R, Thorne CP McMahon, BK (1978). "Design loadings for foundations on shale and sandstone in the Sydney region." Australian Geomechanics Journal, 8, 31-39.

Randolph MF (1994). "Design methods for pile groups and piled rafts." State of the Art Report. XIII ICSMFE, New Delhi, Vol. 5, pp. 61-82.

Randolph MF, Wroth CP (1978). "Analysis of deformation of vertically loaded piles." Journal of the Geotechnical Engineering Division. 104(12), 1465-1488.

Rotta Loria AF, Laloui L (2017). "Thermally induced group effects among energy piles."

Géotechnique. 67(5), 374-393.

Rowe RK, Armitage HH (1987). “A design method for drilled piers in soft rock.” Canadian Geotechnical Journal. 24, 126-142

Saggu R, Chakraborty T (2014). “Cyclic thermo-mechanical analysis of energy piles in sand. Geotechnical and Geological Engineering. 33(2), 321-342.

Seidel JP, Haberfield CM (1994). “Prediction of the variation of bored pile resistance with soil and rock strength.” Australian Geomechanics Journal. 26, 57-64.

Singh R, Bouazza A, Wang B (2015). “Near-field ground thermal response to heating of a geothermal energy pile: observations from a field test.” Soils and Foundations, 55(6), 1412-1426.

Stamatopoulos AC, Kotzias PC (1985). Soil Improvement by Preloading. Wiley, New York.

Stewart MA, McCartney JS (2013). “Centrifuge modeling of soil-structure interaction in energy piles.” Journal of Geotechnical and Geoenvironmental Engineering. 140(4), 04013044.

Suryatriyastuti ME, Mroueh H, Burlon S (2014). “A load transfer approach for studying the cyclic behavior of thermo-active piles.” Computers and Geotechnics. 55, 378–391.

Suryatriyastuti ME, Burlon S, Mroueh H (2015). “On the understanding of cyclic interaction mechanisms in an energy pile group.” International Journal of Numerical and Analytical Methods in Geomechanics. DOI: 10.1002/nag.2382.

Sutman M, Brettmann T, Olgun CG (2014). “Thermo-mechanical behavior of energy piles: full-scale field test verification.” DFI 39th Annual Conference on Deep Foundations, Atlanta, GA. October 21-24, 2014. pp. 1-11. (CD-ROM).

Sutman M, Olgun CG, Laloui L (2018). “Cyclic load–transfer approach for the analysis of energy piles.” Journal of Geotechnical and Geoenvironmental Engineering. 145(1), 04018101.

Wang B, Bouazza A, Singh R, Haberfield C, Barry-Macaulay D, Baycan S (2015). “Post-temperature effects on shaft capacity of a full-scale geothermal energy pile.” Journal of Geotechnical and Geoenvironmental Engineering. 141(4), 04014125-1-12.

Wang W, Regueiro R, McCartney JS (2015). “Coupled axisymmetric thermo-poro-elasto-plastic finite element analysis of energy foundation centrifuge experiments in partially saturated silt.” Geotechnical and Geological Engineering. 33(2), 373–388.

Williams AF, Pells PJN (1981). “Side resistance rock sockets in sandstone, mudstone, and shale.” Canadian Geotechnical Journal. 18(4), 502-513.

Wood CJ, Liu H, Riffat SB (2009). “Use of energy piles in a residential building, and effects on ground temperature and heat pump efficiency.” Géotechnique. 59(3), 287-290.

Wong KS, Teh CI (1995). “Negative skin friction on piles in layered soil deposits.” Journal of Geotechnical Engineering. 121(6), 457-465.

You S, Cheng X, Guo H, Yao Z (2016). “Experimental study on structural response of CFG energy piles.” Applied Thermal Engineering. 96, 640-651.

Zhang P, Mishra B, and Heasley KA (2015). “Experimental investigation on the influence of high pressure and high temperature on the mechanical properties of deep reservoir rocks.” Rock Mechanics and Rock Engineering. 48(6), 2197-2211.

Table 1: Properties of geomaterials

Parameter	Sandy fill	Dense sand	Sandstone	Energy pile
Apparent cohesion (kPa)*	50	20	3000	-
Friction angle (°)	25	30	42	-
Total unit weight (kN/m^3)	18.4	19.2	20.0	25.0
SPT N-Value (blows/300 mm)	70	85	50/25.4 mm	-
Modulus of elasticity, E (MPa)	20	40	500	30000
Poisson's ratio, ν	0.40	0.22	0.20	0.25
Unconfined compressive strength, q_u (kPa)	----	----	12000	----
Adhesion factor, Ψ	----	----	0.672	----
Side shear parameter, β	0.35	0.30	----	----
Coefficient of thermal expansion, α (με/ºC)	----	----	----	13

*Source of cohesion is likely unsaturated conditions near the ground surface

Table 2: Calibrated load-transfer curve parameters for the three energy piles (Case 1)

c	a_s (m)	b_s	a_b (m)	b_b	K_h (GPa/m)	q_u (kPa)
Sandy fill	0.0000002	0.9	----	----	----	----
Dense sand	0.0000002	0.9	----	----	----	----
Sandstone	0.0000003	0.9	0.000002	0.9	----	12000*
Pile 1	----	----	----	----	2.8	----
Pile 3	----	----	----	----	2.0	----
Pile 4	----	----	----	----	2.8	----

* This value of q_u was not used to calculate Q_b due to poor cleanout of the toe, but instead the properties of the sandy fill layer were used to estimate Q_b to represent sandy cuttings

Table 3: Load-transfer curve parameters for Case 2

Layer	a_s (m)	b_s	a_b (m)	b_b	K_h (GPa/m)
Sand	0.0000003	0.9	0.000006	0.9	2.8

Table 4: Load-transfer curve parameters for Case 3

Layer	a_s (m)	b_s	a_b (m)	b_b	K_h (GPa/m)	q_u (kPa)
Rock	0.0000004	0.9	0.000001	0.9	4.0	12000

List of Figure Captions

Figure 1. Discretized pile and a typical pile element: (a) Mechanical load-transfer analysis; (b) Thermo-mechanical load-transfer analysis

Figure 2. Load-transfer curves used in the energy pile analyses in rock: (a) *Q-z* curve with monotonic loading and unloading paths; (b) *T-z* curve with loading and unloading paths

Figure 3. Flow chart of calculation steps

Figure 4. Details of the field experiment site at the US Air Force Academy: (a) Plan view of the locations of the energy piles beneath the grade beam of the building; (b) Schematics of the energy piles including soil layers and instrumentation

Figure 5. Temperature profiles for different average changes in pile temperature for the three piles evaluated by Murphy et al. (2015): (a) Heating; (b) Cooling

Figure 6. Calibrated thermal axial strain during heating: (a) Pile 1 (K_h = 2.8 GPa/m); (b) Pile 3 (K_h = 2 GPa/m); (c) Pile 4 (K_h = 2.8 GPa/m)

Figure 7. Calibrated thermal axial stress during heating: (a) Pile 1 (K_h = 2.8 GPa/m); (b) Pile 3 (K_h = 2 GPa/m); (c) Pile 4 (K_h = 2.8 GPa/m)

Figure 8. Validated thermal axial strain during cooling: (a) Pile 1 (K_h = 2.8 GPa/m); (b) Pile 3 (K_h = 2 GPa/m); (c) Pile 4 (K_h = 2.8 GPa/m)

Figure 9. Validated thermal axial stress during cooling: (a) Pile 1 (K_h = 2.8 GPa/m); (b) Pile 3 (K_h = 2 GPa/m); (c) Pile 4 (K_h = 2.8 GPa/m)

Figure 10. Sensitivity analysis of load-transfer model for ΔT of 18°C: (a) Shaft friction parameter a_s (K_h = 2.8 GPa/m); (b) End bearing parameter a_b (K_h = 2.8 GPa/m); (c) Pile head-structure stiffness K_h

Figure 11. Hypothetical model results for Pile 4 using side shear resistance and end bearing parameters representative of cohesionless soil (K_h = 2.8 GPa/m): (a) Thermal axial strain; (b) Thermal axial stress

Figure 12. Hypothetical model results for Pile 4 using side shear resistance and end bearing parameters representative of rock (K_h = 2.8 GPa/m): (a) Thermal axial strain; (b) Thermal axial stress

Figure 13. Distributions of mobilized side shear stresses (ΔT = 18°C and K_h = 2.8 GPa/m): (a) Calculated values using calibrated parameters from Table 2; (b) Experimental values for Pile 4 along with the predictions from hypothetical cases with different combinations of parameters

Figure 1

Click here to access/download;Figure;Fig 1.tiff

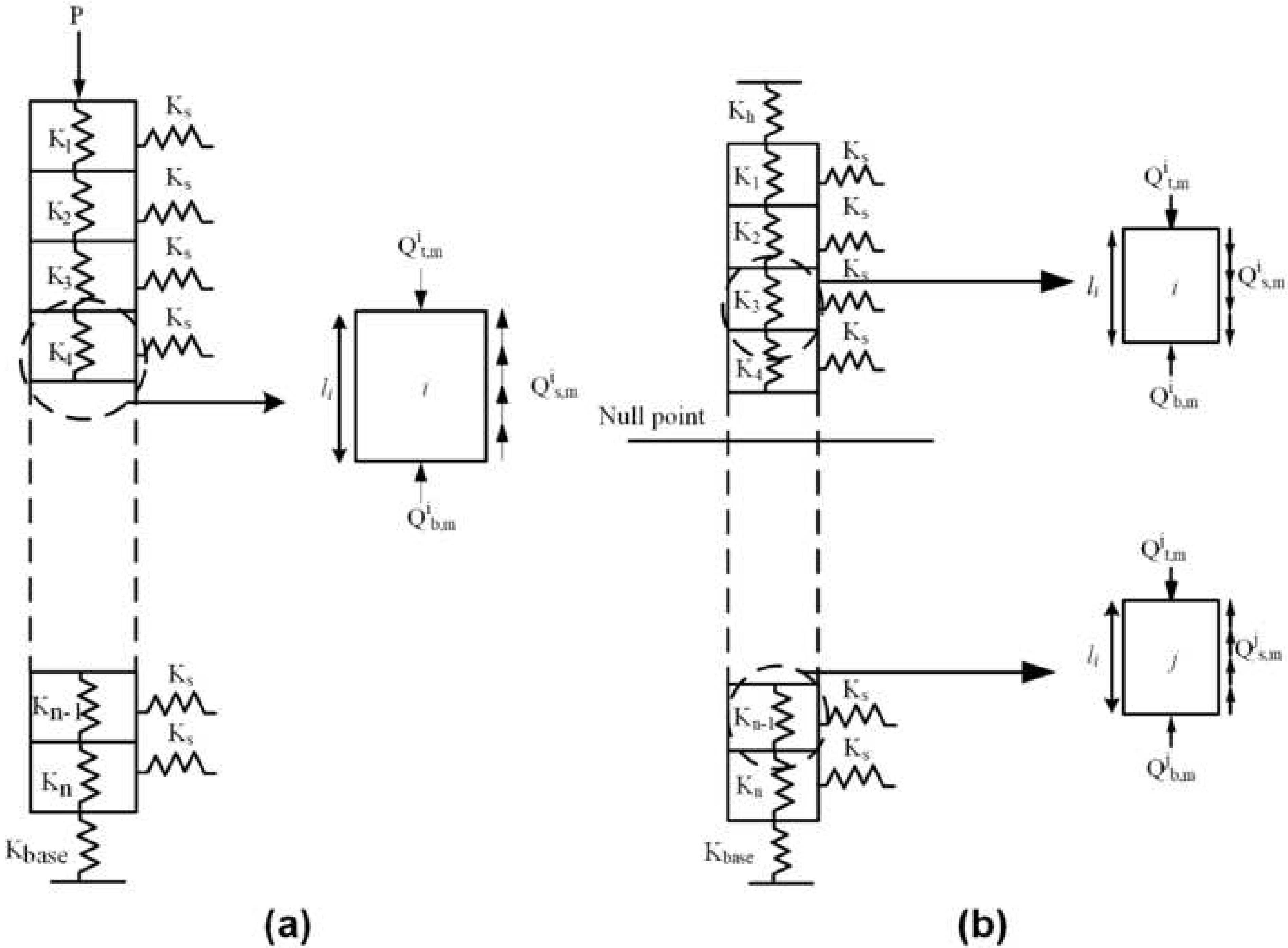

Figure 2

Click here to access/download;Figure;Fig 2.tiff

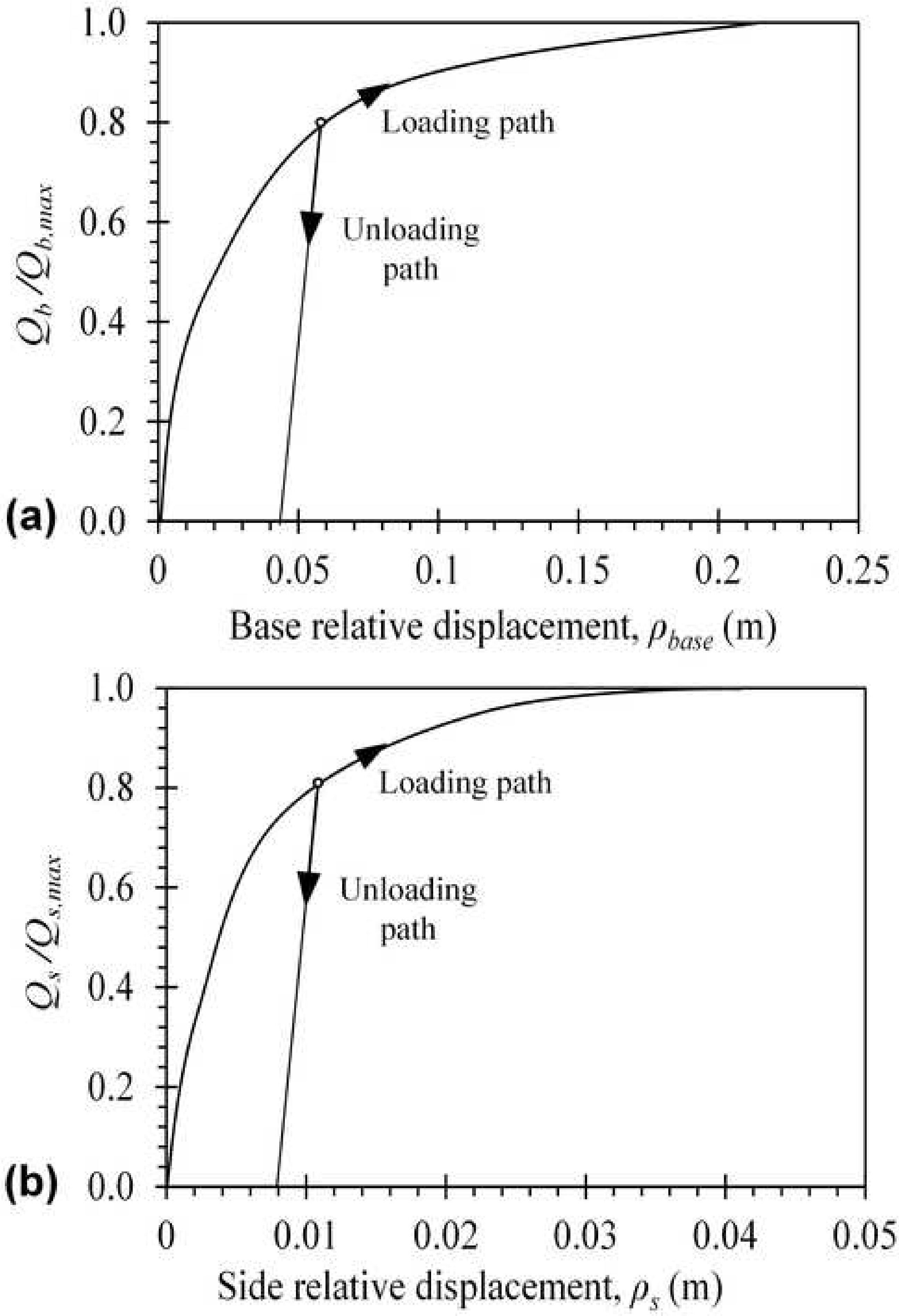

Figure 3

Click here to access/download;Figure;Fig.3.tiff

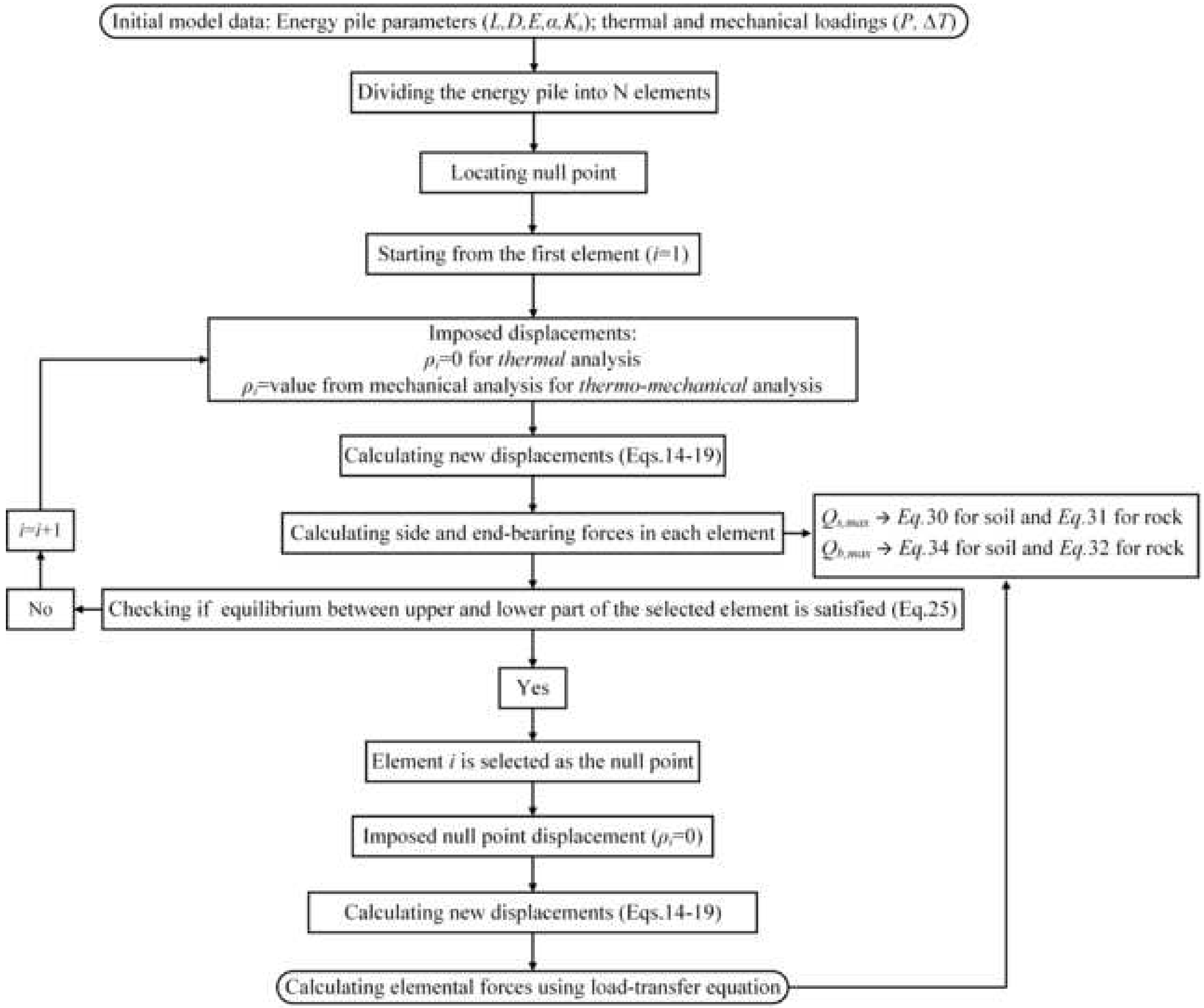

Figure 4

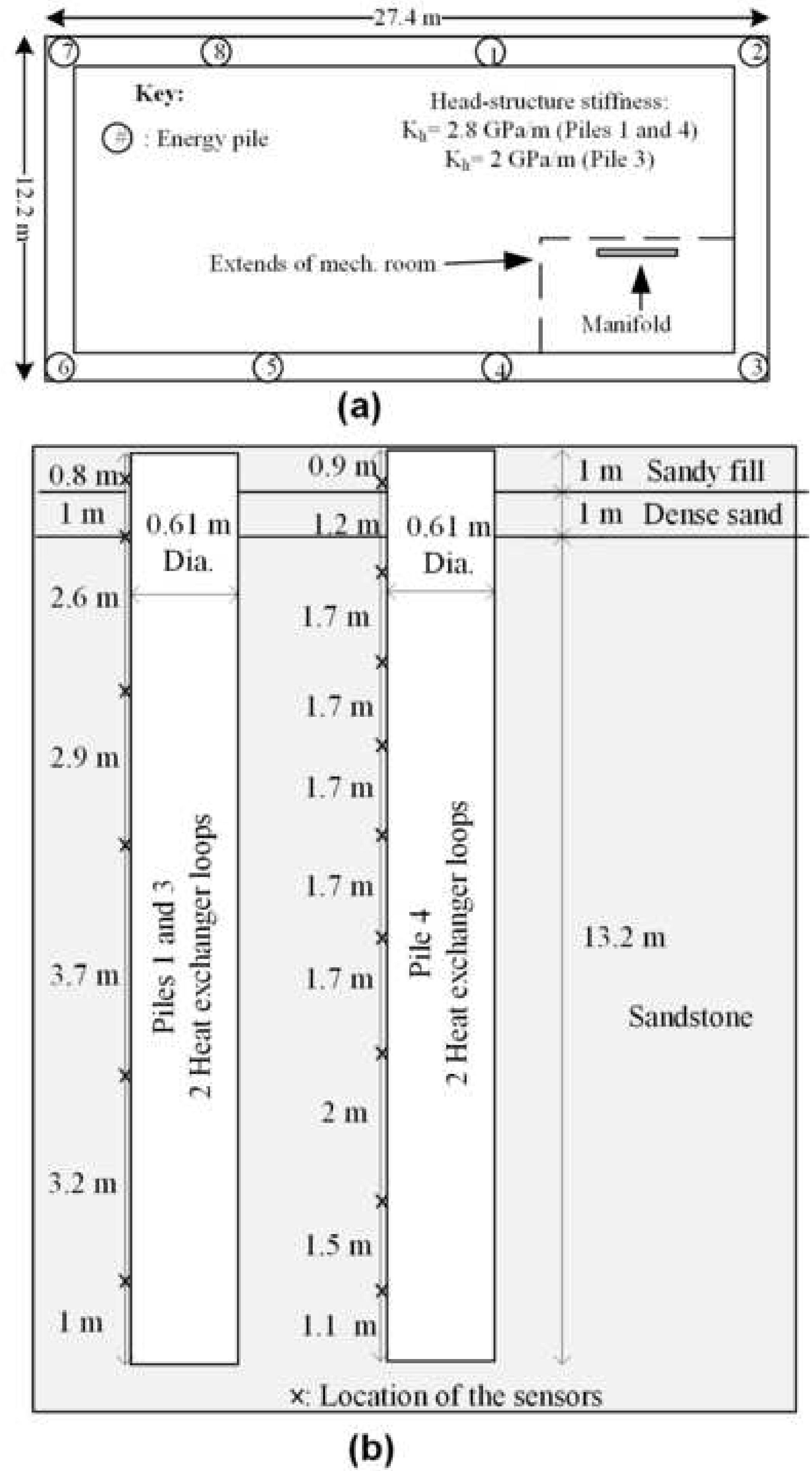

27.4 m
12.2 m
Key:
: Energy pile
Head-structure stiffness:
K_h = 2.8 GPa/m (Piles 1 and 4)
K_h = 2 GPa/m (Pile 3)
Extends of mech. room
Manifold
(a)
0.8 m
1 m
2.6 m
2.9 m
3.7 m
3.2 m
1 m
0.61 m
Dia.
Piles 1 and 3
2 Heat exchanger loops
0.9 m
1.2 m
1.7 m
1.7 m
1.7 m
1.7 m
1.7 m
2 m
1.5 m
1.1 m
0.61 m
Dia.
Pile 4
2 Heat exchanger loops
1 m Sandy fill
1 m Dense sand
13.2 m
Sandstone
×: Location of the sensors
(b)

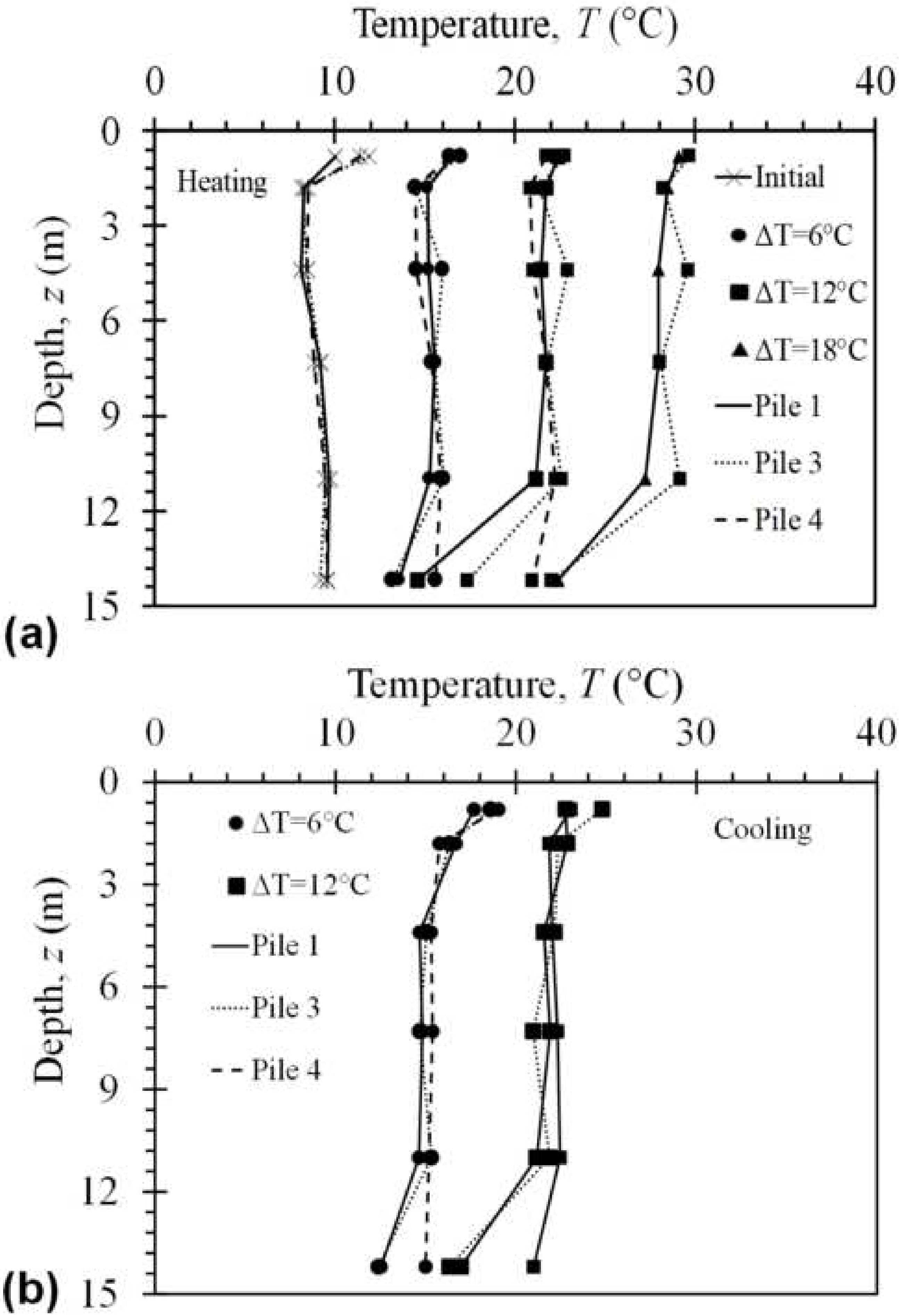
Temperature, T (°C)
0
10
20
30
40
Depth, z (m)
0
3
6
9
12
15
Heating
Initial
ΔT=6°C
ΔT=12°C
ΔT=18°C
Pile 1
Pile 3
Pile 4
(a)
Temperature, T (°C)
0
10
20
30
40
Depth, z (m)
0
3
6
9
12
15
Cooling
ΔT=6°C
ΔT=12°C
Pile 1
Pile 3
Pile 4
(b)

Figure 6

Click here to access/download;Figure;Fig.6.tiff

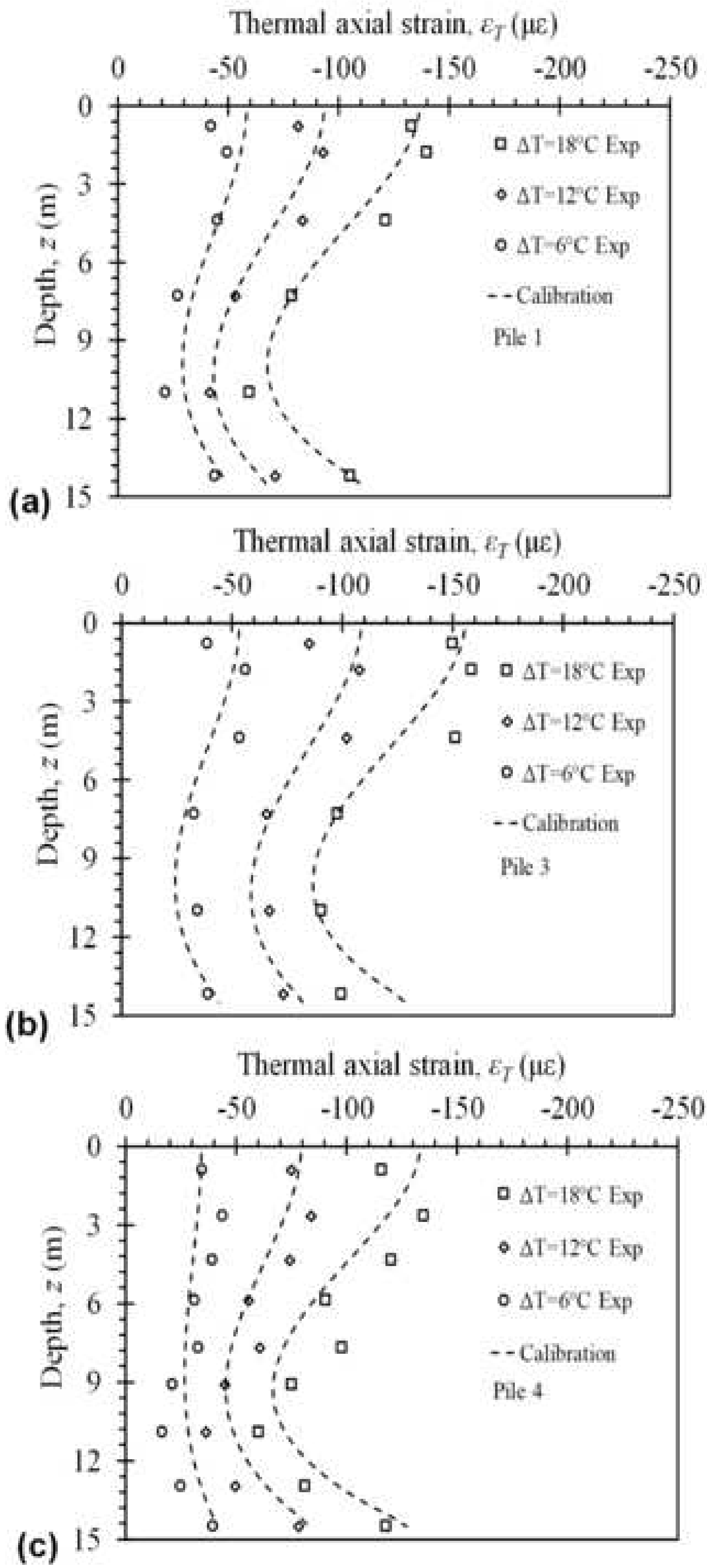

Figure 7

Click here to access/download;Figure;Fig.7.tiff

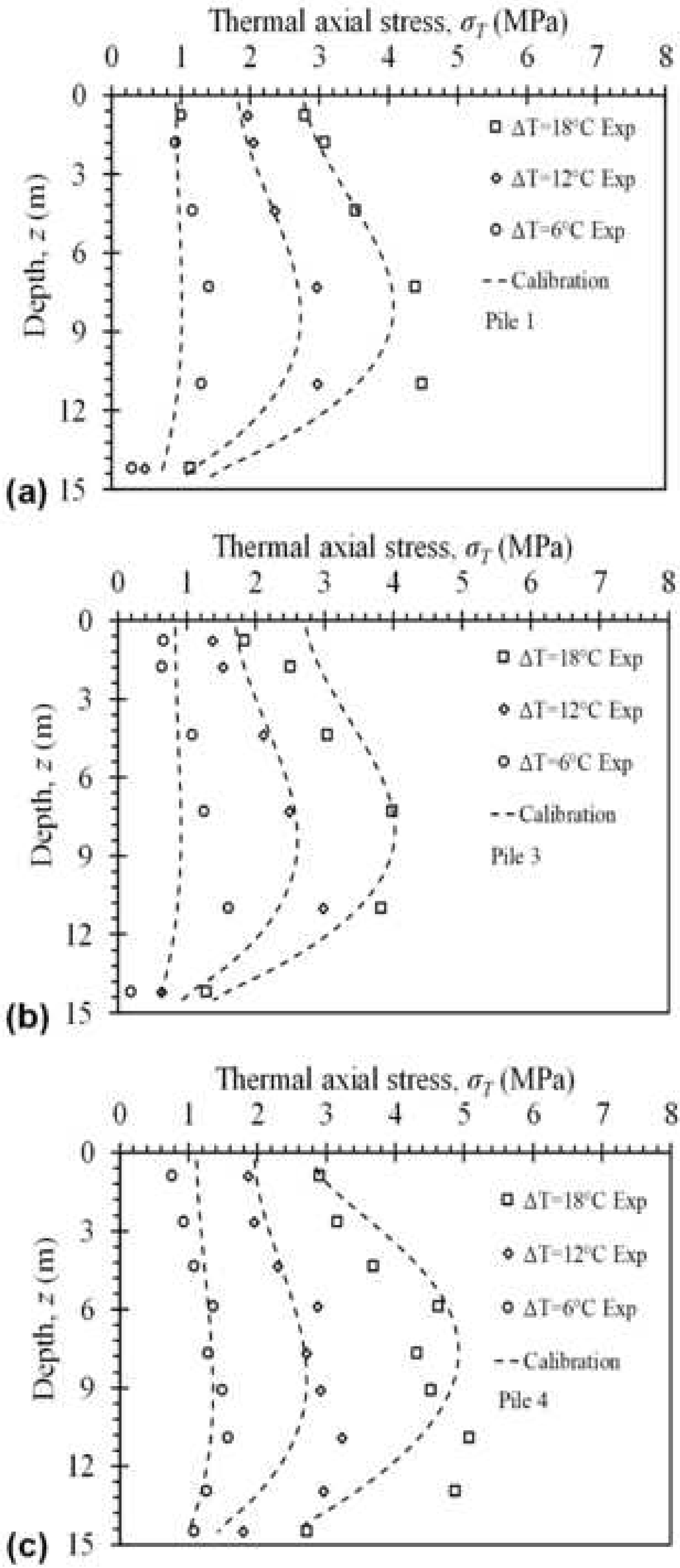

Figure 8

Click here to access/download;Figure;Fig.8.tiff

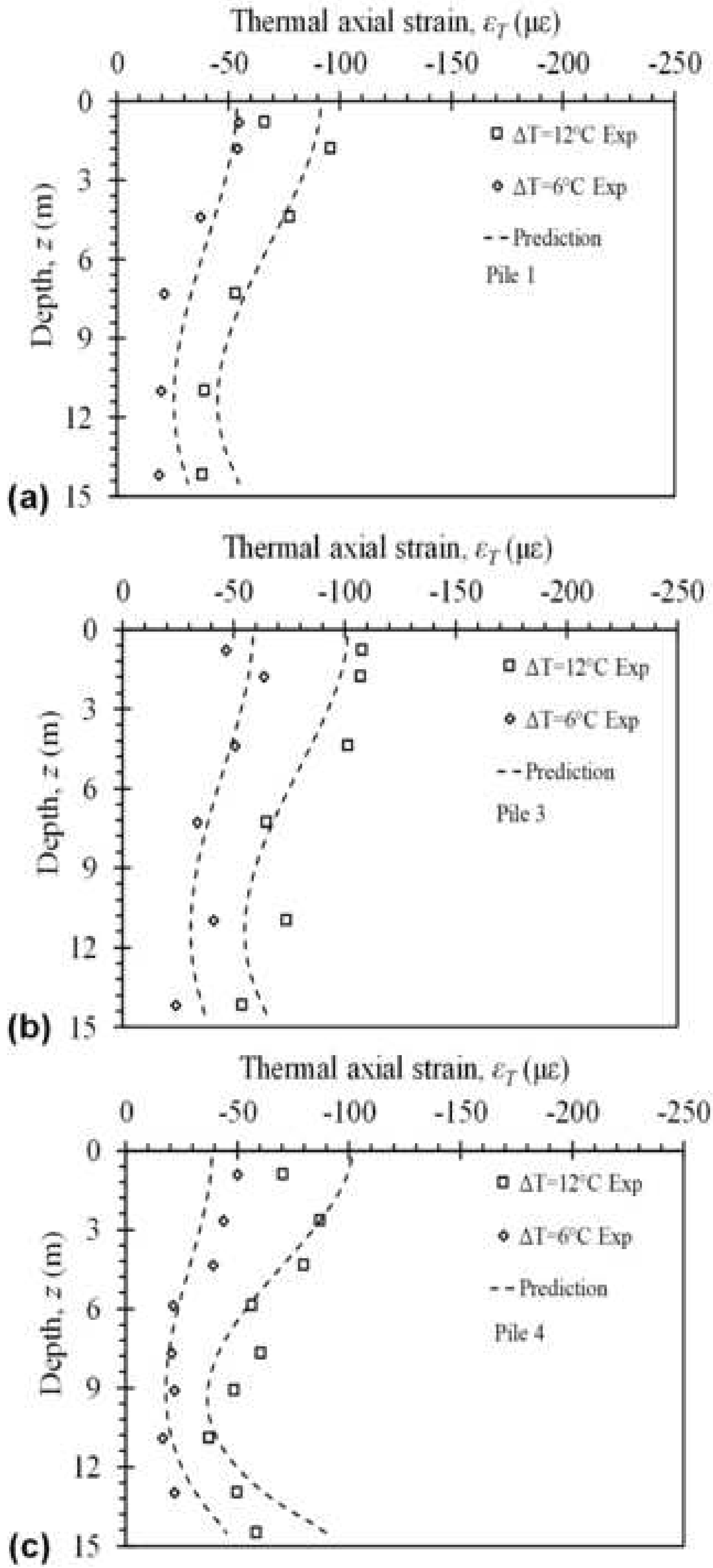

Figure 9

Click here to access/download;Figure;Fig.9.tiff

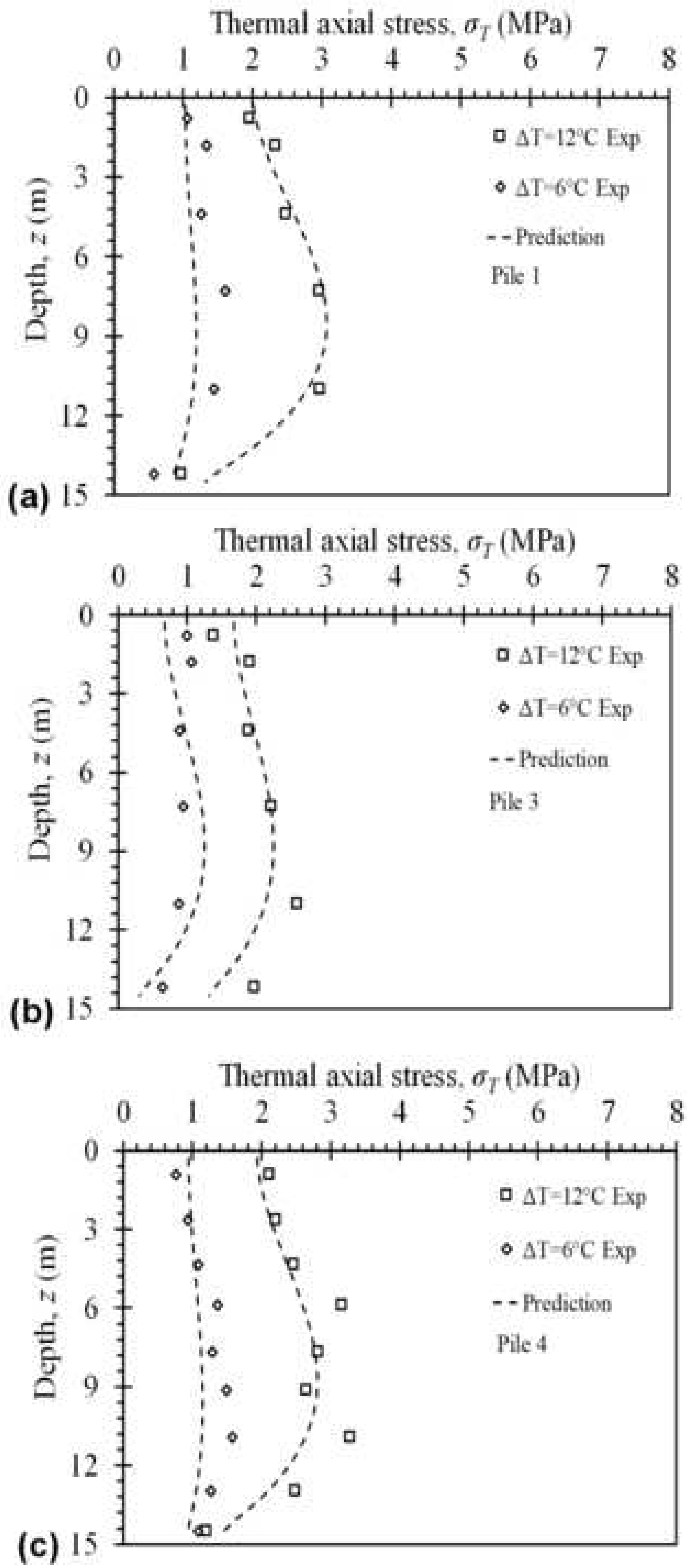

Figure 10

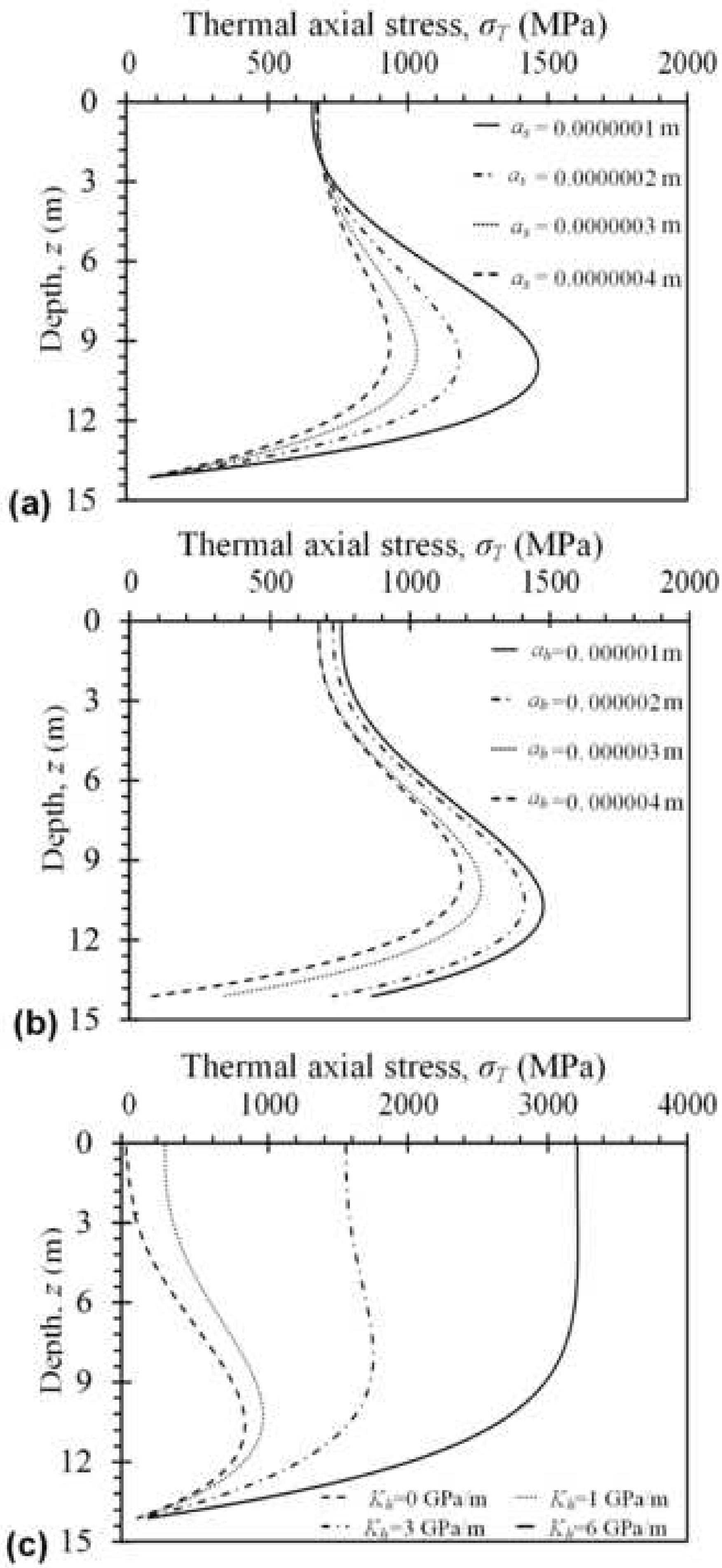

Thermal axial stress, σ_T (MPa)
0
500
1000
1500
2000
Depth, z (m)
0
3
6
9
12
15
a_s = 0.0000001 m
a_s = 0.0000002 m
a_s = 0.0000003 m
a_s = 0.0000004 m
(a)
Thermal axial stress, σ_T (MPa)
0
500
1000
1500
2000
Depth, z (m)
0
3
6
9
12
15
a_b=0.000001m
a_b=0.000002m
a_b=0.000003m
a_b=0.000004m
(b)
Thermal axial stress, σ_T (MPa)
0
1000
2000
3000
4000
Depth, z (m)
0
3
6
9
12
15
K_b=0 GPa/m
K_b=1 GPa/m
K_b=3 GPa/m
K_b=6 GPa/m
(c)

Figure 11

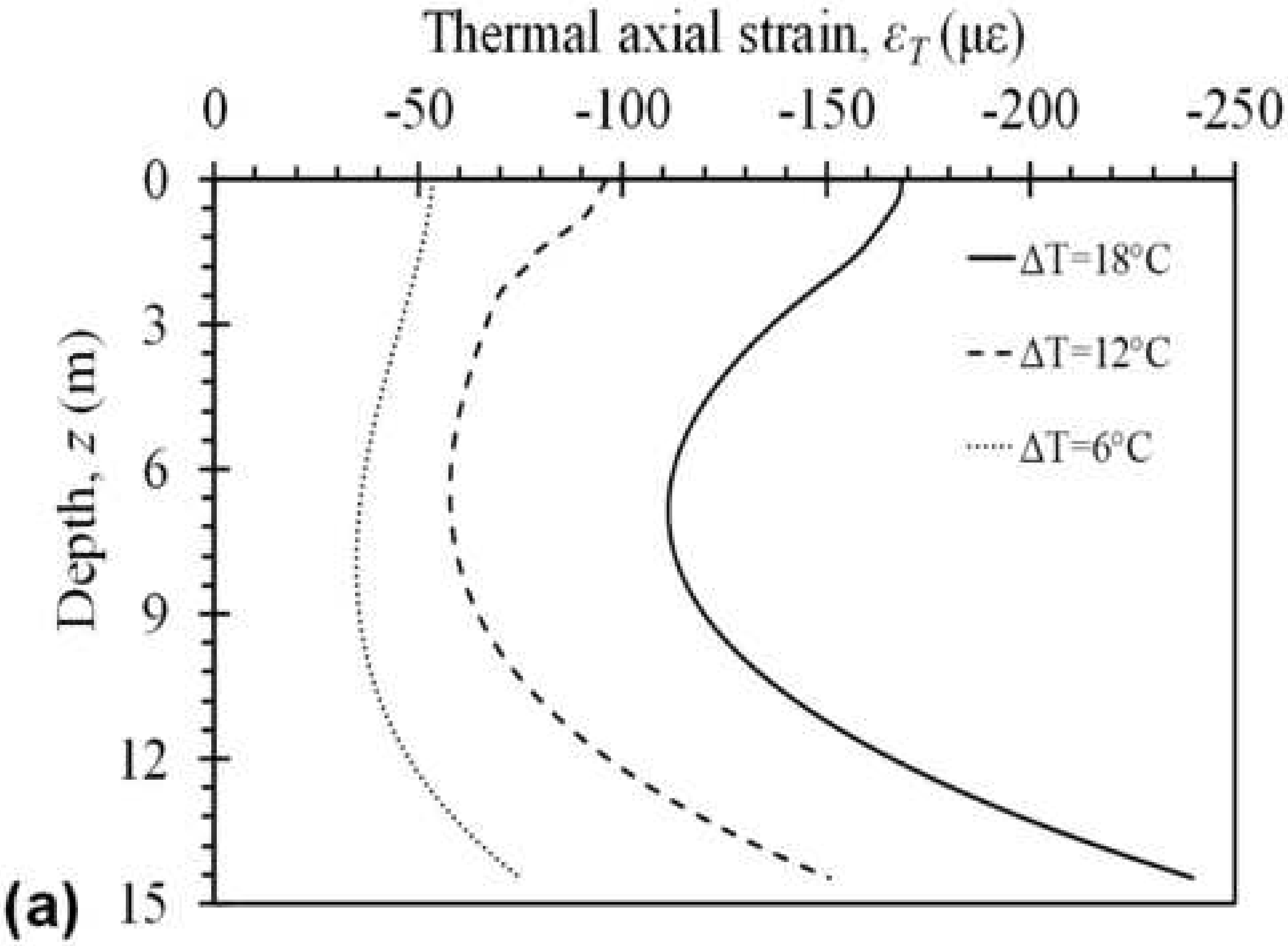
Thermal axial strain, ε_T (με)
0
-50
-100
-150
-200
-250
Depth, z (m)
0
3
6
9
12
15
ΔT=18°C
ΔT=12°C
ΔT=6°C
(a)

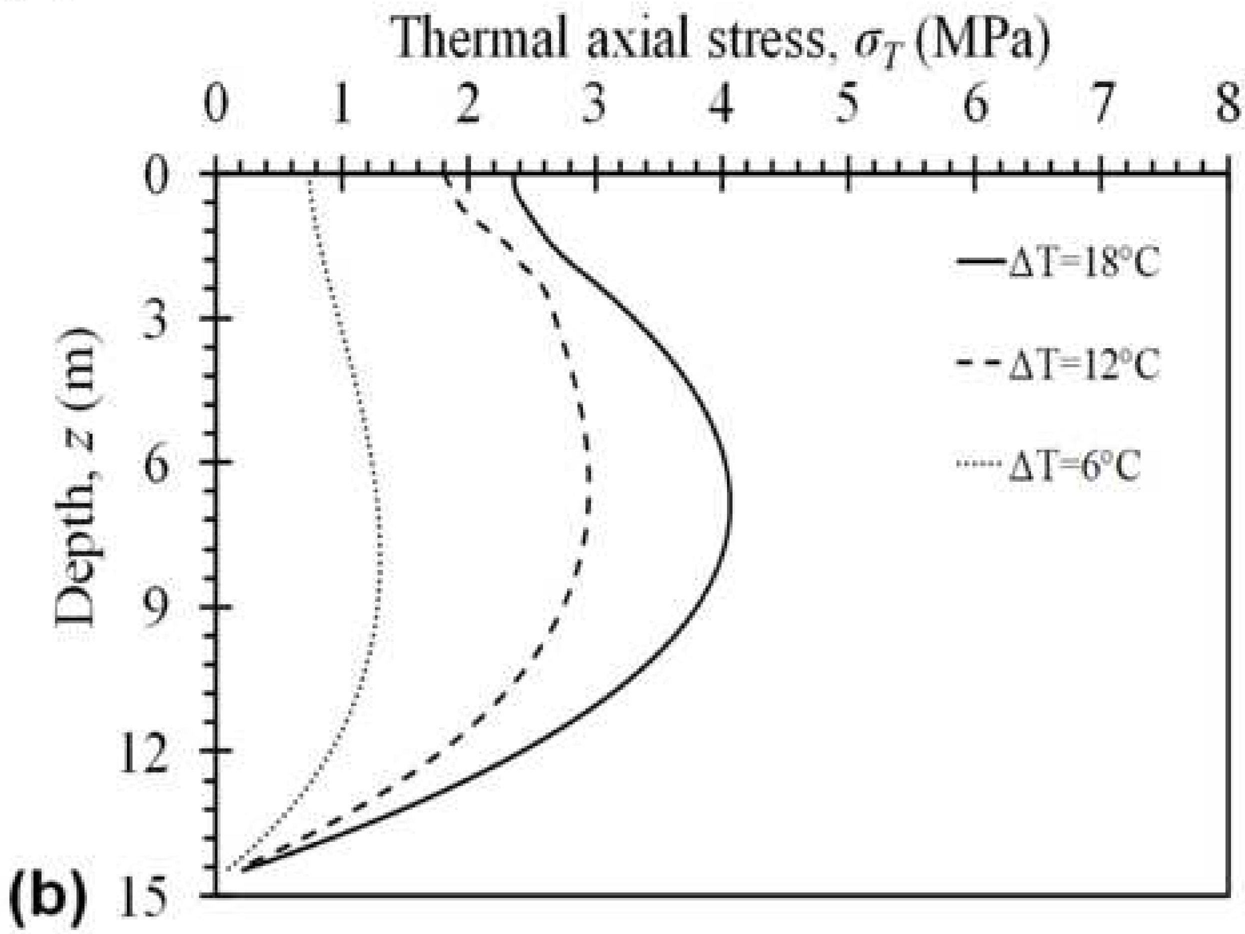
Thermal axial stress, σ_T (MPa)
0
1
2
3
4
5
6
7
8
Depth, z (m)
0
3
6
9
12
15
ΔT=18°C
ΔT=12°C
ΔT=6°C
(b)

Figure 12

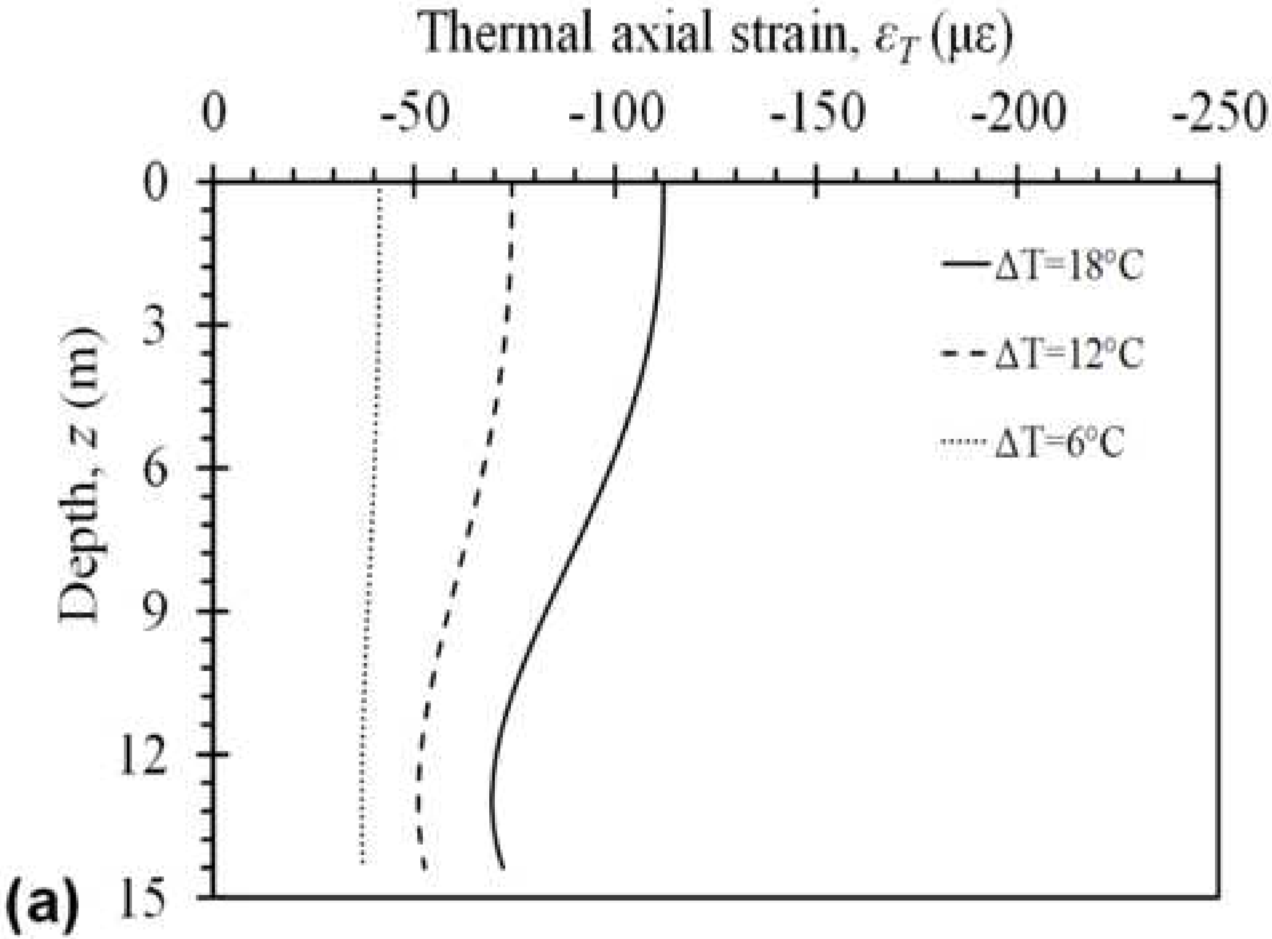
Thermal axial strain, ε_T (με)
0
-50
-100
-150
-200
-250
Depth, z (m)
0
3
6
9
12
15
ΔT=18°C
ΔT=12°C
ΔT=6°C
(a)

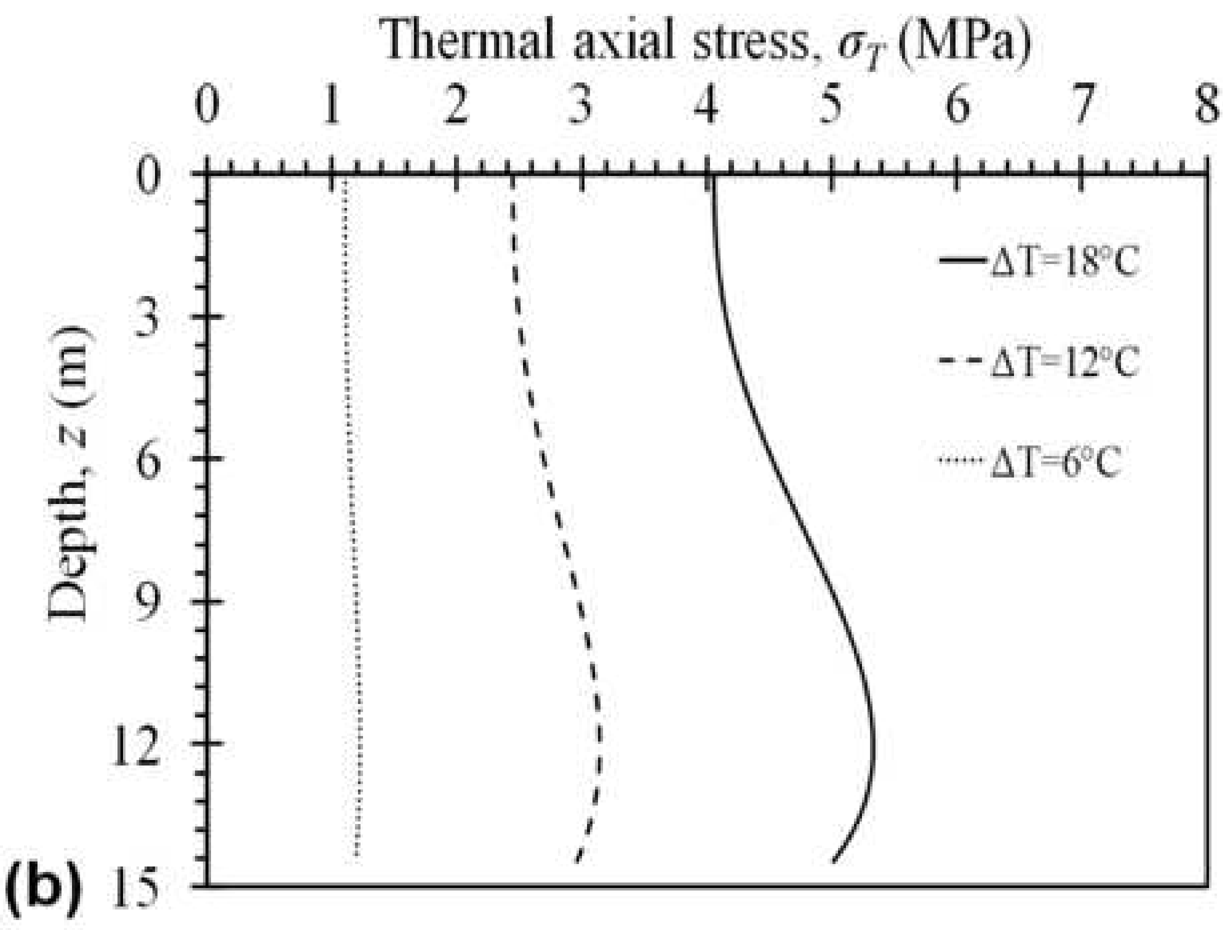
Thermal axial stress, σ_T (MPa)
0
1
2
3
4
5
6
7
8
Depth, z (m)
0
3
6
9
12
15
ΔT=18°C
ΔT=12°C
ΔT=6°C
(b)

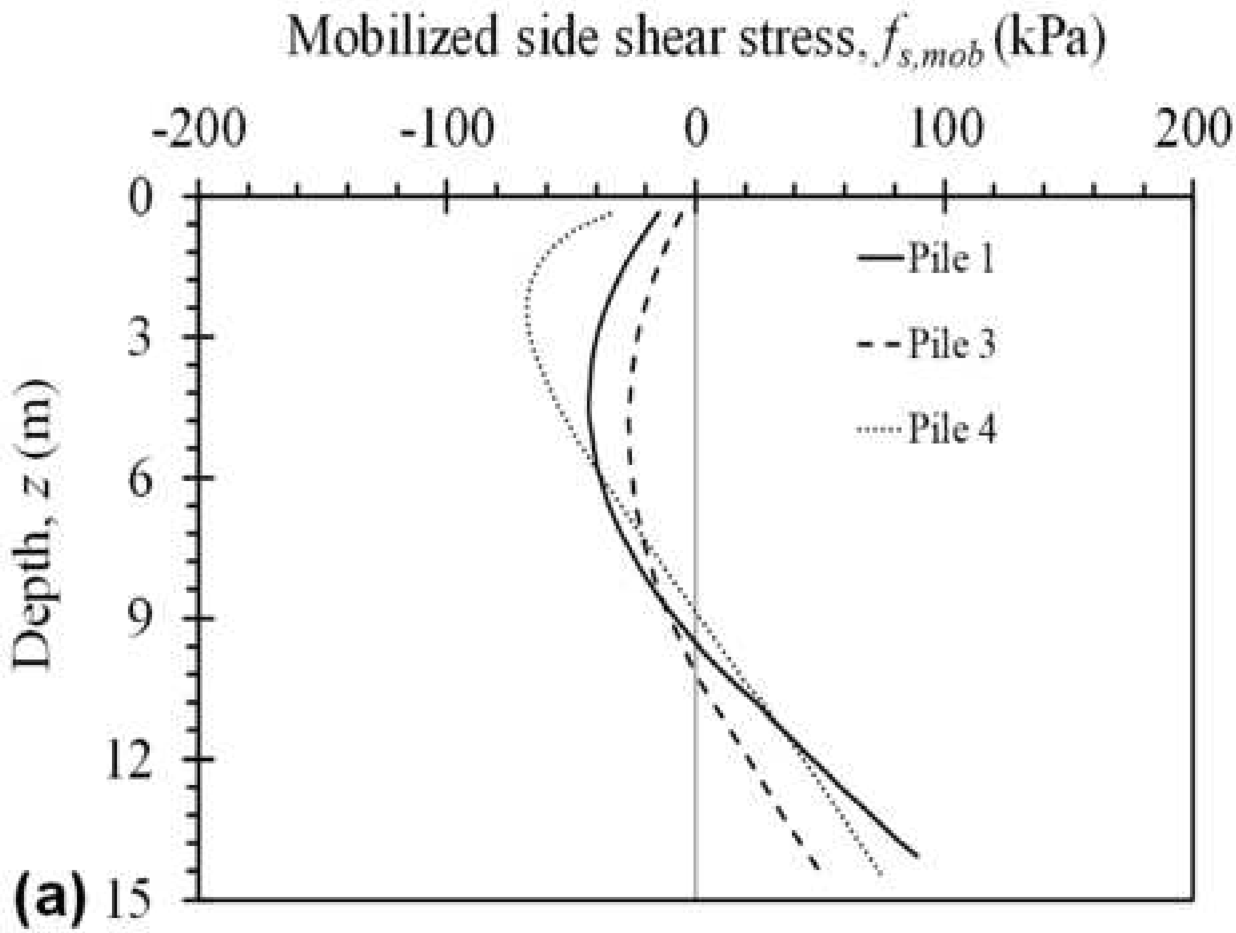
Mobilized side shear stress, $f_{s,mob}$ (kPa)
-200
-100
0
100
200
0
3
6
9
12
15
Depth, z (m)
Pile 1
Pile 3
Pile 4
(a)

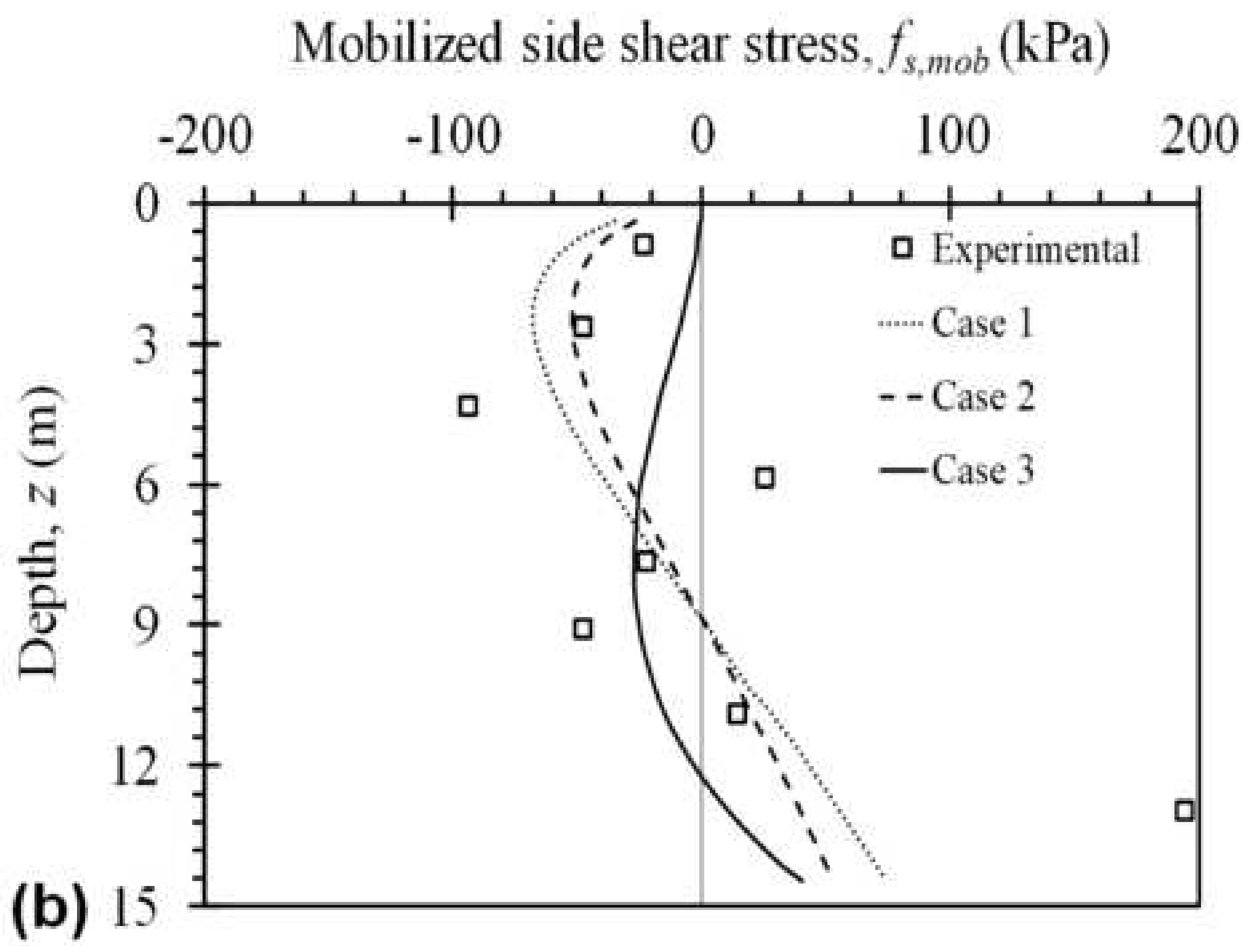
Mobilized side shear stress, $f_{s,mob}$ (kPa)
-200
-100
0
100
200
0
3
6
9
12
15
Depth, z (m)
Experimental
Case 1
Case 2
Case 3
(b)